Engineering Failure Analysis 165 (2024) 108775

Contents lists available at ScienceDirect

Engineering Failure Analysis

journal homepage: www.elsevier.com/locate/engfailanal

# Mechanical and metallurgical characterization of contact fatigue mechanisms in ADI spur gears

Andrea Casaroli, Marco Boniardi, Edoardo Conrado, Carlo Gorla, Carlo Crispino, Riccardo Gerosa, Barbara Rivolta *

*Department of Mechanical Engineering, Politecnico di Milano, Via la Masa 1, 20156 Milano, Italy*

ARTICLE INFO

*Keywords:*
Austempered ductile iron
Spur gear
Contact fatigue
Failure mechanism

ABSTRACT

Surface pitting of gear teeth flanks is one of the most common causes of gear failure. The increase of the contact fatigue strength of gears is usually achieved through the development of new combinations of materials and heat-treatment processes. Austempered Ductile Iron (ADI) is one of the results of this research field that leaded to a material which is replacing conventional steel in many mechanical applications. This paper shows the experimental results obtained from tests performed on ADI spur gears in order to characterize the contact fatigue crack nucleation and growth and understand the possible interaction with the graphite spheroids and casting defects. Using a four-square test rig, it was carried out a systematic monitoring of the evolution of the damage, collecting several images concerning crack development at gear surfaces. At the end of the tests several metallurgical analyses of surface and sub-surface areas were performed to understand the fracture mechanism at the base of the pitting failure in ADI. All experimental analyses were complemented by theoretical calculations, useful for a better understanding of the phenomenon.

## 1. Introduction

Gears are machine elements used to transmit rotating motion between two shafts, normally with a constant ratio. Surface pitting of gear teeth flanks is one of the most common causes of gear operational failure. This mode of failure leads to crack initiation at or under the contact surface, and may subsequently lead to damage varying in extent from microscopic pitting to severe spalling. Pitting is a fatigue phenomenon characterized by a gradual failure of the contact surfaces [1–3] and is observed as the formation of small surface breaking or subsurface nucleated cracks growing under repeated contact loading. Eventually, the crack becomes large enough for unstable growth to occur, which causes the material surface layer to break away. In the modern gear industry, the increase of the pitting strength of gears is achieved mainly through the development of new combinations of materials and heat-treatment. One of these is the austempering of nodular iron, which allows the production of a competitive material called Austempered Ductile Iron (ADI). The advantages of ADI, compared to steel, are the production of near-net shapes cast components, the reduction of the machining costs, lower density (about 10 % less than steels), high damping and self-lubricating properties, noise and wear reduction [4], mechanical properties easy to calibrate with a low-cost and low energy demanding heat treatment [4–6]. Moreover, the modern casting techniques make the production costs very low in comparison with forged or hobbed gears. M. Yamanaka et Al. [7] concluded

* Corresponding author.
*E-mail address:* barbara.rivolta@polimi.it (B. Rivolta).

https://doi.org/10.1016/j.engfailanal.2024.108775
Received 24 June 2024; Received in revised form 28 July 2024; Accepted 13 August 2024
Available online 14 August 2024

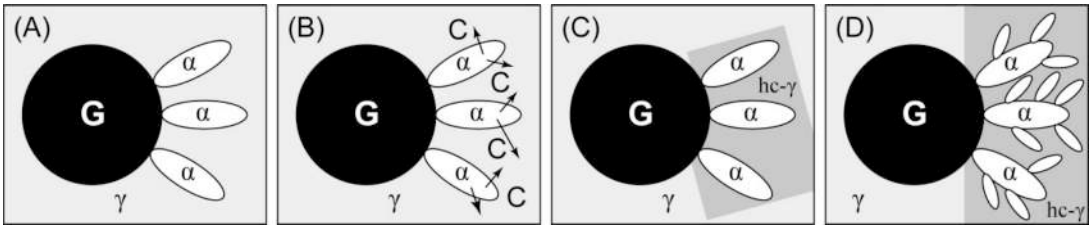


**Fig. 1.** Schematic representation of the ausferrite transformation [9]. The final microstructure (D) shows ferrite sheaves, grown beside the graphite nodules, surrounded by stabilized austenite.

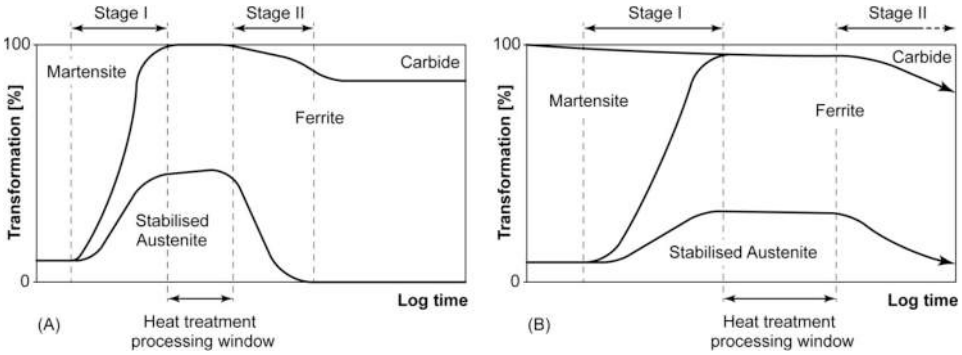


**Fig. 2.** Schematic representation of the ausferrite transformation at different heat treatment temperatures: (A) high austempering temperature and (B) low austempering temperature [10].

that the fatigue strength-cost ratio of ADI is similar to that of hobbed and carburized gears, but still lower of that of forged and carburized gears. Even though the ADI fatigue resistance-cost ratio is very competitive, this material is generally not recommended when alloys with very high strength are required (most of the power-transmission gears are still made of steel). Nevertheless, some ADI can nowadays reach UTS values higher than 1,600 MPa, a limit sufficient to support the stresses imposed by the majority of mechanical applications. L. Magalhaes et al. [8] and J. Han et al. [9] compared the resistance to scuffing of ADI, other cast irons and steels. They found that the ADI samples showed the highest resistance. About bending and contact fatigue, instead, hardened steel gears have higher performance as reported by M. Yamanaka et al. [10].

The microstructure of ADI consists of nodular graphite scattered in a matrix formed by ferrite needles and stabilized austenite. The mechanical characteristics do not depend on the properties of the single phases only. They are the result of the synergy among the austenite and ferrite regions and the microstructure refinement driven by the austempering treatment: higher the austempering temperature, greater the ductility and the toughness and lower the mechanical resistance. Very fine carbides may be found as precipitates in the ferrite phase for low austempering temperature. Stabilized austenite is saturated with carbon and doesn't transform into martensite when it is cooled to room temperature. Due to close similarity with the bainite obtained in steels, this microstructure is known as bainitic structure, although some researchers called it ausferrite [11–14]. Fig. 1 describes the ausferrite transformation. After the austenitization, the matrix is carbon-saturated austenite. At the beginning of the austempering, the carbon-saturated austenite transforms into ferrite (Fig. 1a). The first ferrite needles nucleate near the austenite-graphite interface. These ferrite needles are supersaturated with carbon; therefore, the carbon atoms diffuse from the ferrite needles to the surrounding austenite (Fig. 1b), resulting in carbon content increasing in austenite (Fig. 1c). Further, ferrite needles nucleate on the already existing ferrite needles, so that the entire structure of the ferrite phase is sheaf-like (Fig. 1d). This growth of ferrite further increases the carbon content in austenite. The final microstructure shows ferrite sheaves, grown beside the graphite spheroids, surrounded by stabilized austenite [12].

This microstructure is usually classified as lower or upper ausferrite. Austempering temperatures in the range 260–300 °C produce lower ausferrite, a compact structure with very dense ferrite needles and low austenite content, maximizing tensile strength and hardness. Upper austenite forms above 300 °C and contains larger blocks of stabilized austenite. Ferrite needles are larger and more scattered into the austenite matrix, resulting in more ductile materials, reaching elongation after fracture up to 12 %.

Once the austempering temperature has been selected, the austempering time must be chosen to optimize properties through the formation of a stable structure. At short austempering times, there is insufficient diffusion of carbon into the austenite to stabilize it, and martensite may form during cooling to room temperature. The resultant microstructure would have higher hardness, but lower ductility and fracture toughness. Excessive austempering times can result in retained austenite decomposition into ferrite and carbide, which will exhibit lower strength, ductility, and fracture toughness [13]. This undesirable transformation is commonly referred to as stage II transformation while the formation of retained austenite and ferrite is commonly known as stage I transformation (Fig. 2). Austempering time should be selected within the range of heat treatment processing window to avoid the formation of martensite and decomposition of retained austenite, in order to have a desired ADI matrix structure. In practice, it is rather difficult to define heat

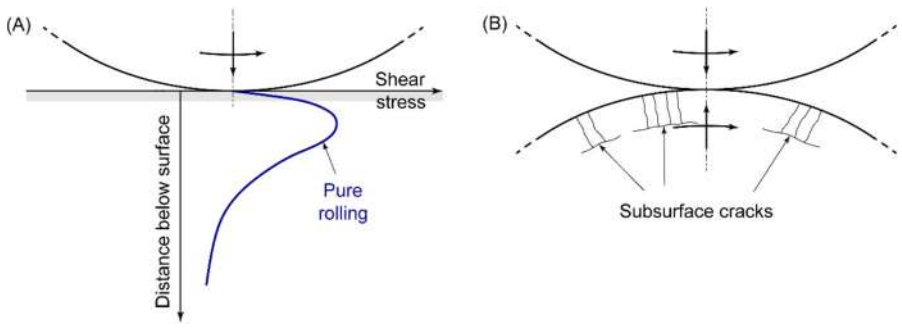


**Fig. 3.** Two surfaces in contact under pure rolling condition, (A) shear stress distribution, (B) location and orientation of subsurface cracks.

treatment processing window as shown in Fig. 2.

In alloyed ductile iron, as a consequence of segregation during solidification, the end of stage I in less alloyed zones and the beginning of stage II in more alloyed zones may shrink or overlap one another eliminating the heat treatment processing window. Even though the chemical composition is generally subordinated to the mechanical properties, it respects the following limits: C=3.3 %–3.8 % C, Si = 1.8 %–2.8 % S, Mn ≤0.6 %, S≤0.03 %, P≤0.10 % Fe as balanced. Moreover, the addition of Mg is very important to activate the graphite spheroidization process. Finally, other alloying elements, such as Cu, Ni and Mo can be added.

Silicon is one of the most important alloying elements in ADI, because it promotes graphite formation, decreases the solubility of carbon in austenite, increases the eutectoid temperature and inhibits the carbide formation delaying the austempering transformation. Higher silicon content increases the impact strength of ADI and lowers the ductile to brittle transition temperature. Silicon should be controlled closely within the range of 2.4 %–2.8 % [14].

Manganese improves the hardenability; its addition is useful to prevent pearlite formation in thick cast-sections. Copper stabilises austenite by acting as a barrier to carbon diffusion at the austenite-graphite boundary [15].

For heavy-section casting, copper, nickel, molybdenum and other alloying elements are added to increase hardenability, improve the grain refinement and the microstructural homogeneity. However, these elements can easily segregate at the grain boundaries, forming carbides and leading to shrinkage problems and fracture toughness reduction [16,17].

Being a relatively recent material, some ADI properties are still not well characterised, such as its behaviour under heavy contact loads like the one present in spur gears. For example, there is lack of understanding about the pitting formation on gears surface. In fact, there are many involved factors such as: the contact stress level, the tooth profile, the relative contact speed, the surface finishing, the lubrication conditions and all the parameters related to the material such as the shape, the distribution and the dimension of the graphite nodules, the microstructural inhomogeneity and the casting defects [18,19].

The aim of this research work is to give a systematic analysis of the mechanisms of contact fatigue-crack growth in Austempered Ductile Iron spur gears. Crack initiation and propagation, the influence of graphite nodules and casting defects on the pitting gears life are some of the aspects that will be investigated in this work. For this purpose, some ADI gears have been tested at different load level in a mechanical recirculating power test bench. An exhaustive photographic documentation analysis was done, following the evolution of the damage on the gears surface during the contact fatigue tests. In this way, it was possible to study the variation of the pitting features in different zones of the tooth flank. Furthermore, optical and electronic microscopes were used to perform surface and sub-surface post-test analysis, obtaining information about the crack propagation and the metallurgical characteristics. The experimental analyses were complemented by theoretical calculations which have been correlated to the obtained results.

## 2. Contact fatigue damage mechanism in ADI

Different failure modes can occur on gear surface, sometimes occurring in combination with each other [20]; however, each type of failure has detailed characteristics.

Davis [21] divides gear failures into non-lubrication-related failures and lubrication-related failures. Non-lubrication-related failures are then divided into failures caused by overload and bending fatigue, while the lubrication-related failures are divided into Hertzian fatigue (micro-pitting, pitting, spalling), wear, and scuffing. For our purposes, we will concentrate on the lubrication-related failures and in particular on the contact fatigue failure modes (Hertzian fatigue).

The surface contact fatigue is one of the most common modes of gear failure encountered in practice. Whenever two bodies having curved surfaces are pressed together, point or line contacts generates very small circular or elliptical contact areas, resulting in very high contact stresses with the maximum shear stresses at a specific depth below the surface [21], as showed in Fig. 3a. When the contacting stresses are cyclic, as is the case on the active flanks of gear teeth, the shear stresses cause material degradation by plastic deformations in sub-surface material eventually leading to crack nucleation.

The damage due to contact fatigue in gear teeth usually occurs in one of these three areas [22]:

- along the pitch-line,
- in the addendum (i.e. above the pitch-line),

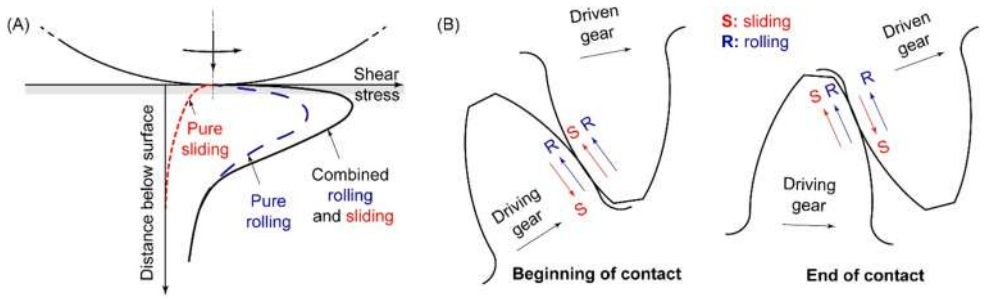


**Fig. 4.** (A) Stress distribution on and below two surfaces in contact in sliding-rolling conditions. (B) Combination of sliding and rolling in gear teeth.

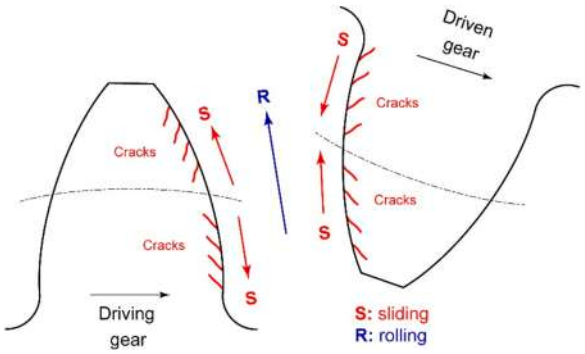


**Fig. 5.** Schematization of rolling (R), sliding (S) and crack propagation directions in the drive and driven gear teeth.

- in the dedendum (i.e. below the pitch line).

Along the pitch-line, only pure rolling stresses exist, while away from the pitch line, both rolling and sliding stresses are experienced. The stress distribution resulting from pure rolling conditions at the pitch-line is shown in Fig. 3a. Cracks initiate at the point of maximum stress and propagate essentially parallel to the surface. As shown in Fig. 3b, continued rolling may cause the cracks to move up towards the contact surface, resulting in metal detachment from surface. The formed pits are generally very small. These pits may not progress beyond their point of origin [22]. Pure rolling conditions prevail when the rolling speed of the two curved bodies are the same. However, if the speed is different, sliding is introduced and alters the stress distribution. The sliding speed is defined as the difference between the rolling speeds of the meshing teeth. At a given point on the line of action, they can be calculated according to Eqs. (1) and (2):

$$V_p = \omega_p{}^*\rho_p \tag{1}$$

$$V_w = \omega_w{}^*\rho_w \tag{2}$$

$\omega_p$, $\omega_w$ and $\rho_p$, $\rho_w$ are the angular rotation speeds and the curvature radii for the pinion and the wheel respectively.

The rolling speed of the pinion, $V_p$, and that of the wheel, $V_w$, increase linearly from zero at the first contact points to a maximum at the end of the contact. The rolling is beneficial, because it introduces the lubricant between the contacting teeth and increases the thickness of the oil film. Depending on the relative speed of the contacting bodies, rolling and sliding may occur in the same or in the opposite direction. The first condition is called positive, the latter negative sliding. For negative sliding, present in the dedendum, the rolling and the sliding forces acting on the material surface have opposite direction, resulting in stresses higher than those encountered in positive sliding [23,24]. In this region the gear tooth surface is subjected to the highest contact forces. In this area, pitting is very severe and can evolve to bending fatigue. The modified stress distribution at the surface and the sub-surface region, resulting from combined rolling and sliding, is shown in Fig. 4a. The position of maximum shear stress moves closer to the contact zone, and hence the crack initiation occurs near/at the surface. Gear teeth have complex combinations of sliding and rolling, which vary along the profile of each tooth, as illustrated in Fig. 4b.

In practice, contact fatigue damage will first occur in the dedendum of the smaller gear (which is usually the driving gear) [25,26] that undergo more revolutions and therefore more stress cycles.

Another region of contact fatigue damage is the lowest point of single tooth contact, i.e. the point where the contact regards the tip of the matching tooth [27,28]. The very small contact area generates high stresses even under limited loads. The positive sliding conditions in these regions, together with the high stresses and high sliding speeds, lead to rapid initiation of damage.

Because of the negative and positive sliding conditions, the cracks that can eventually nucleate on the teeth flank, point toward the

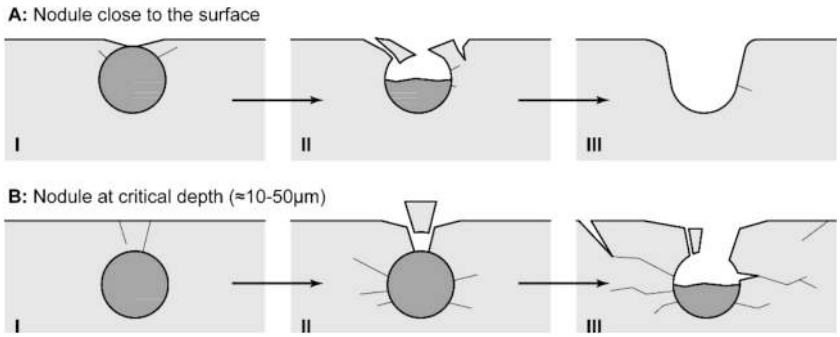


**Fig. 6.** Typical evolution of cracks around graphite nodules located near the surface of an ADI. (A) nodules close to the surface and (B) nodules at some critical depth (approximately from 10 μm to 50 μm) [29].

pitch line of the pinion and diverge from the pitch line of the wheel. This behaviour is related to the sliding speed between the two meshing teeth.

Fig. 5 shows the rolling (R) and sliding (S) directions. The contact on the driving gear or pinion tooth begins near the root and moves towards the tip where it ends. The slip moves away from the pinion pitch line. The contact on the driven gear or wheel tooth instead starts at the tip and ends at the root.

The fracture mechanism of components subject to rolling contact fatigue requires two stages: crack nucleation and propagation. Murakami [29] demonstrated the fundamental role played by defects, such as non-metallic inclusions, graphite nodules, porosity, casting flaws and bad surface finishing on the fatigue resistance. After a high number of fatigue tests varying the flaw size, he developed some methods to convert them into equivalent cracks. Murakami defined two main classes, i.e. inner and surface defects. The equivalent crack was calculated as the square root of the convex area that envelops the defect. Moreover, he proposed a method to understand when two or more nearby defects can be considered a sole cluster. Murakami considered the surface roughness as well, since it increases the stress locally and hence it can promote the fatigue failure. He proposed some expression to convert the surface condition after the machining operation into an equivalent crack. This theory is often employed to study the fatigue behavior of composite materials, cast irons and castings in general, sintered steels and additive manufactured components. All these materials are characterized by a matrix with intrinsic "flaws" such as reinforcing particles, inner porosity, bad surface finishing and, in the case described in this paper, graphite spheroids.

Assuming that inside the material a micro-crack already exists, the fracture mechanic principles can be applied as reported in Eq. (3).

$$\Delta K = Y\Delta\sigma\sqrt{\pi a} \tag{3}$$

$\Delta K$ is the applied stress intensity factor range

$\Delta\sigma$ is the applied stress range.

$a$ is the equivalent defect length,..$a = \sqrt{Area}$

$Area$ is the area of the convex figure including the defect.

$Y$ is a geometrical factor.

The conversion of the defects described previously generally results in short equivalent cracks. In this case, Murakami reported that $Y = 0.65$ for surface defects and $Y = 0.5$ for inner defects. As confirmed experimentally, surface defects are more critical than inner ones. For this reason, in case of contact fatigue stresses, the presence of surface or sub-surface graphite nodules promotes the crack nucleation reducing the fatigue life of the gear. As reported in the technical literature [30–32], small, round and well distributed graphite nodules, results in higher fatigue resistance. This can be justified easily considering that smaller spheroids can be converted in shorter equivalent cracks.

Moreover, lubrication is a further issue to be considered carefully: when its effect decreases, the friction forces increases making the actual stress condition more severe. Moreover, an increased friction contribution can generate a local temperature increase with a consequent modification of the material mechanical and wear properties. Compared with the ADI gears, the case-hardened steel ones have better fatigue resistance. This can be justified considering that the absence of particles and pores in the metal matrix, especially in the hardened zone, makes the equivalent crack very short and essentially related to the surface roughness only. Nevertheless, it must be remarked that the very high surface hardness makes the case-hardened gear more sensitive to the notch effect associated to the surface roughness or other flaws.

K. Aslantaş et al. [33] reported that crack nucleation resistance of ADI is lower than that of steel, because ADI behaves as a composite: cyclic loading weakens the interface bond between the matrix and the nodule, generating microcracks that start from a graphite nodule and grow creating, together with the others, a network of cracks.

Moreover, Greno et al [34] demonstrated that ADI has higher crack propagation resistance respect to martensitic steel of similar strength. This difference can be attributed to the different crack path. The fatigue crack propagation in ADI is characterized by continuous changes in direction, caused by nodules near the crack tip. Furthermore, ausferrite leads to a complex crack propagation

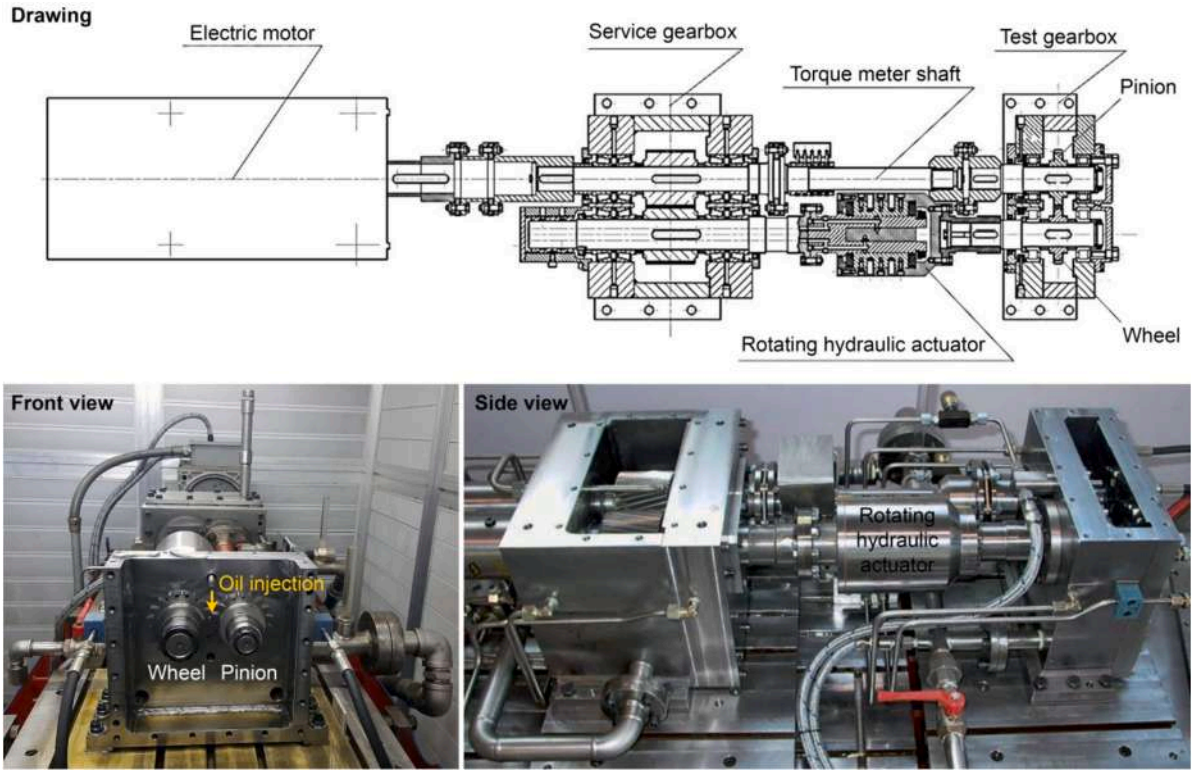


**Fig. 7.** Schematic representation and photographs of the mechanical recirculating power test bench used for the contact fatigue tests.

which increases energy absorption. Finally, the retained austenite may transform into martensite, generating a compressive residual stress, which reduces the crack opening and causes an additional consumption of energy, which, in turns, is not available for crack growth.

As said before, the casting defects and the graphite nodule size and distribution are important characteristics to be considered. Rebasa et al [30], Dommarco et al. [31] and Gupta et al. [35] show, by numerical simulation, that the smaller is the discontinuity, the lower is the contact pressure peak, leading to higher contact fatigue life. Therefore, it is important to have high number of small nodules in order to increase the fatigue life. Magalhães et al. [36] theorized two different types of crack growth, depending on nodules depth from surface and local stress field (Fig. 6).

1. *Condition n. 1: superficial graphite nodules.* They are located on or just below the surface and don't influence the contact fatigue performance considerably. The superficial graphite nodules cause an early cracking of ADI surfaces subjected to high contact pressure. Graphite nodules tend to be ejected, forming cavities which acquire smooth edges. Magalhães et al. [36] didn't found significant fatigue cracks starting from those cavities.
2. *Condition n. 2: sub-superficial graphite nodules.* They are located 10 μm – 50 μm below the surface and can form a large cavity, with a strong stress concentration, when subjected to high contact pressure. These defects can act as starting point for crack propagation, which is favoured by the lubricant compressed inside them.

According to Magalhães et al. [37], casting defects (mainly microscopic foundry defects such as porosities or shrinkage cavities) are one of the main causes for fatigue crack nucleation in ADI. When located near the surface, these defects cause the crack initiation and consequent possible catastrophic spalling.

In the technical literature, several authors [25–27,35–37] proposed different theories to explain the contact fatigue crack mechanism in ADI; sometimes these theories conflict with each other. This is due to the high number of involved factors (shape, distribution and dimensions of graphite nodules, microstructural inhomogeneity and casting defects, lubrication and load condition, gear geometry etc.). The influence of each of these factors is yet not fully understood and further investigation is needed to clarify these points, especially for high-pressure contacts, typical of spur gears.

## 3. Materials and methods

Before the tests, the gears surface roughness, microstructure and hardness were evaluated.

Contact fatigue tests were performed on the mechanical recirculating power test bench showed in Fig. 7. This back-to-back gear rig,

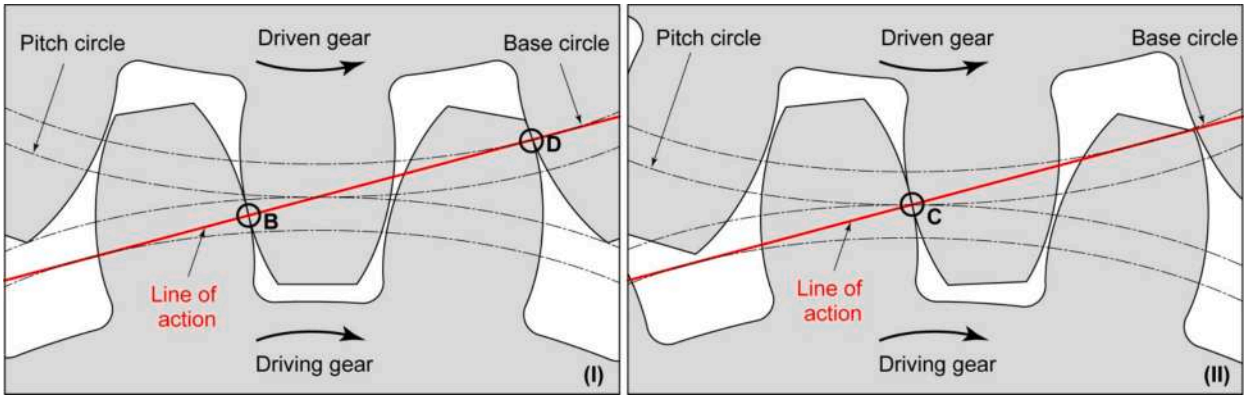


**Fig. 8.** Contact points along the line of action at the pitch (C) and at the inner point of single pair tooth contact for the driving gear (B) and the driven gear (D).

**Table 1**
Main characteristics of the four-square test rig used for the contact fatigue tests.

| | |
|---|---|
| **Centre distance** | 91.5 mm |
| **Maximum torque** | 1,000 Nm |
| **Maximum rotational speed** | 3,000 rpm |
| **Lubrication type** | Spray or bath lubrication |
| **Oil injection/bath temperature** | Up to 120 °C |

**Table 2**
Geometrical properties of the gears (pinion and wheel) used for the contact fatigue tests.

| **Description** | **Symbol** | **Unit** | **Formula** | **Value** | |
|---|---|---|---|---|---|
| | | | | Pinion | Wheel |
| **Operating centre distance** | a | (mm) | | 91,5 | |
| **Face width** | b | (mm) | | 14 | |
| **Module** | m | (mm) | | 5 | |
| **Transverse pressure angle** | $\alpha_t$ | (°) | | 20 | |
| **Helix angle** | β | (°) | | 0 | |
| **Number of teeth** | $Z_1/Z_2$ | (−) | Set value | 17 | 18 |
| **Profile shift coefficient** | $X_1/X_2$ | (−) | | 0,4753 | 0,4450 |
| **Tip diameter** | $d_{a1}/d_{a2}$ | (mm) | | 99,509 | 104,206 |
| **Tool basic rack profile** | | | | | |
| **Addendum per unit module** | $H_{aP0}$ | (−) | | 1,294 | |
| **Root fillet radius per unit module** | $\rho_{fP0}$ | (−) | | 0,375 | |
| **Reference diameter** | $d_1/d_2$ | (mm) | $zm$ | 85 | 90 |
| **Base diameter** | $d_{b1}/d_{b2}$ | (mm) | $dcos(\alpha)$ | 80 | 84,572 |
| **Working pitch diameter** | $d_{w1}/d_{w2}$ | (mm) | $\frac{d_b}{\cos(\alpha_w)}$ | 88,885 | 94,114 |
| **Working pressure angle** | $\alpha_w$ | (°) | $arcos\frac{d_{b1}+d_{b2}}{2a}$ | 26,023 | |
| **Gear ratio** | u | (−) | $\frac{Z_2}{Z_1}$ | 1,0588 | |
| **Transverse base pitch** | TBP | (mm) | $\frac{\pi d_{b1}}{Z_1}$ | 14,7606 | |
| **Transverse contact ratio** | $\varepsilon_\alpha$ | (−) | Refer to Ch.4 | 1,35 | |
| **Accuracy grade** | ISO AG | (−) | | 5 | |

with a centre distance of 91.5 mm as the typical FZG type configuration, recirculates power in a closed-loop torque regenerative arrangement, also known as four-square configuration.Fig. 8..

The bench is actuated by an asynchronous motor, controlled by an inverter, which has to provide power only to overcome the frictional losses in the system (usually 10 % of the circulating [38,39]). Test gears are connected at one end to helical slave gears and at the other end to two parallel shafts. One shaft is divided in two parts with the hydraulic loading system in between. This rotating hydraulic actuator allows the application and variation of the torque also during the operation of the rig, thus enabling test at variable load amplitude. The other shaft is equipped with a strain gage system for torque measuring. The bench is equipped with two independent lubrication circuits, one dedicated to the service gearbox and the hydraulic actuator, and the second for the test gearbox, in

**Table 3**
Test conditions used for the contact fatigue tests on gear B1 and B2.

| Id. | Gear | Torque (Nm) | Speed (rpm) | Pinion rotation | Oil temperature | Oil feed | Flank (Z17) | Flank (Z18) |
|---|---|---|---|---|---|---|---|---|
| **B1-200-L** | **B1** | 200 | 3000 | Counter clockwise | 60 °C | Oil injection in mesh direction | Left | Left |
| **B1-200-R** | **B1** | 200 | 3000 | Counter clockwise | 60 °C | Oil injection in mesh direction | Right | Right |
| **B1-280-L** | **B2** | 280 | 3000 | Counter clockwise | 60 °C | Oil injection in mesh direction | Left | Left |
| **B1-280-R** | **B2** | 280 | 3000 | Counter clockwise | 60 °C | Oil injection in mesh direction | Right | Right |

**Table 4**
Mechanical properties requirements according to ISO 17804 for ADI grade JS-800–10 [41].

| Grade | $R_m$ [MPa] min. | $R_s$ [MPa] min. | A% [%] min. (t ≤ 30 mm) | Hardness [HBW] |
|---|---|---|---|---|
| JS-800–10 | 800 | 500 | 10 | 250–310 |

**Table 5**
Chemical composition and heat treatment parameters for the investigated material.

| C [%] | Mn [%] | Si [%] | Mg [%] | S [%] | P [%] | Fe [%] | Austenitization | Austempering |
|---|---|---|---|---|---|---|---|---|
| 3.45 | 0.18 | 2.43 | 0.061 | 0.019 | 0.012 | Bal. | 920 °C, 2 h | 380 °C, 2 h |

which the lubricant temperature can be set independently. Table 1 summarize the test rig main characteristics.

The test gears were designed expressly for this experimental study. The geometrical properties, summarized in Table 2., were defined to favour the pitting damage and to avoid others type of failures (micro pitting, scuffing or bending fatigue). The gear is constituted by a 17 teeth pinion and an 18 teeth wheel. This choice was made to avoid that one tooth of the pinion meshes always the same tooth of the wheel. The profile shift coefficient was set to increase the bending strength and to reduce the pitting resistance.

Tests were performed on two couples of gears (pinion and wheel), named B1 and B2, in order to understand the origin and propagation of the contact fatigue mechanism. A second objective is to define the influence of ADI microstructure on gear performances at different stress levels.

For this purpose, tests were stopped when the pitting/spalling damage extension, evaluated by the parameter $(\%) = \frac{Damagedarea}{Totalarea} \bullet 100$, was higher than 4 % of the active surface on a single tooth flank in accordance with AGMA 939 Standard [40]. Run out was set to $6.5{\cdot}10^6$ cycles.

Two load levels were used at 200 Nm and 280 Nm. For all tests, the pinion speed was set at 3,000 rpm and the gear pair was lubricated with an oil jet in the mesh direction of AGIP Blasia 220 at constant temperature of 60 °C. This oil contains EP additives to increase scuffing resistance.

All the tested gears were submitted to a short running-in, conducted at speed of 1,500 rpm, torque 100 Nm and with oil temperature of 60 °C, for a total of 100.000 cycles. Running-in is useful to adapt the teeth profiles to each other, smoothing surfaces and favouring load distribution. The test conditions are summarized in Table 3..

Tests were regularly stopped to monitor the damage evolution. At each stop, all teeth were cleaned to remove the oil and subjected to camera inspection. The camera is a Canon Eos 400D equipped with a macro-camera lens type "Canon EF 100 mm F/2.8 Macro USM EOS". The magnification was set to 1:1 while aperture, shutter speed and ISO were set one time to have the same optimal exposure parameter for all pictures.

The camera support system was specifically designed for the test rig to obtain pictures always from the same distance, angulation and exposure from the teeth. Only in this way, it was possible to evaluate the damage evolution on the teeth surfaces correctly. The images were also used to quantify the pitting area extension.

The tested spur gears were made in ADI JS-800-10 grade [41]. The typical mechanical properties are shown in Table 4..

The delivered material didn't allow the machining of specimens for tensile tests. For this reason, only hardness tests were employed to verify the compliance of the investigated material with the nominal grade characteristics. They were performed on the same samples used for metallographic analysis by Brinell HBW2.5/187.5 scale. Finally, micro-indentation HV0.5 tests were carried out in the ausferritic matrix as well. The gears chemical composition and heat treatment parameters is reported in Table 5.

Before the beginning of the contact fatigue tests, the microstructure was evaluated on a third pinion, of the same material and shape, not used for the tests. Cutting was carried out very carefully to prevent microstructural modifications. Polishing was performed with abrasive papers and 3 μm/1μm diamond cloths. Microstructure was observed by LEICA® DM4000M optical microscope before and after etching by Nital2 reagent ($HNO_3$, 2 ml and ethanol 98 ml).

After casting, the gears teeth were machined by grinding. The surface finishing has a strong influence on the contact fatigue life,

**Table 6**
Profilometer technical data and measurement condition used for roughness tests.

| Technical Data | | Measurement Parameters | |
|---|---|---|---|
| **Profilometer** | Mahr PGK | **Cut-Off** | 0.8 mm |
| **Tracer Point** | MFW-250 | **Wavelength ($\lambda_c$)** | |
| **Sensing Arm** | 6851805 | **Roughness** | 0.8 mm |
| **Tip Radius** | 2 μm | **Sampling Length ($l_r$)** | |
| **Sliding Block** | NO | **Roughness** | 4.0 mm |
| **Upper Threshold** | +250 μm | **Evaluation Length ($l_n$)** | |
| **Lower Threshold** | −250 μm | **Roughness** | 5.6 mm |
| **Filter** | Gaussian | **Traversing Length ($l_t$)** | |
| **Translation Direction** | To translating unit | **Translation Speed** | 0.5 mm/s |
| **Return Stroke** | No contact | | |

because roughness behaves as a stress concentration for crack initiation [42]. For this reason, roughness was measured before starting the tests in the radial direction on the middle plane of the teeth flank. The measurements were done following the UNI EN ISO 21920-3:2022 standard [43]. Profilometer technical data and measurement condition are summarized in Table 6..

The tests were performed on four teeth for each pinion and wheel of gear B1 and B2; measurements were replicated four times for each tooth.

## 4. Results and discussion

### 4.1. Contact stresses calculation

The calculation of the contact stresses is very important to fully understand the pitting formation in spur gears. The maximum contact pressure and the half contact width are fundamental to identify the amplitude and the position of the maximum shear stress. Many researchers theorize that maximum shear stress and its location are responsible for the surface fatigue failure; therefore, it is important to calculate them accurately.

The standard procedure used to estimate the contact stresses in spur gears is to simplify two teeth in contact as two rotating cylinders. The radius of the two equivalent cylinders is equal to the curvature radius of the teeth in the specific contact point [44]. Three different standardization bodies (ISO, AGMA, and DIN) propose different procedures to estimate the contact pressure and the consequent stresses. The standard used for this research paper is the ISO 6336 *"Calculation of load capacity of spur and helical gears"* [45] This standard is divided in many parts, but for our purpose we have used only the first two (part 1: *"Basic principles, introduction and general influence factors"* and part 2: *"calculation of surface durability (pitting)"*); both parts are based on the Hertzian surface compressive stress theory.

The ISO 6336-2 standard [45] provides equations (4–6) to estimate the contact pressure at the pitch point (C) and at the inner point of single pair tooth contact for pinion, or driving gear (B) and wheel, or driven gear (D).

$$P_C = \frac{\sigma_{H0}}{Z_\varepsilon Z_\beta} = Z_H Z_E \sqrt{\frac{F_t}{d_1 b}\frac{u+1}{u}} [MPa] \tag{4}$$

$$P_B = \frac{Z_B \sigma_{H0}}{Z_\varepsilon Z_\beta} = Z_B P_C [MPa] \tag{5}$$

$$P_D = \frac{Z_D \sigma_{H0}}{Z_\varepsilon Z_\beta} = Z_D P_C [MPa] \tag{6}$$

Where:

- $P_C$ is the Hertzian contact pressure at the pitch point $C$
- $P_B$ is the Hertzian contact pressure at the inner point $B$ of single pair tooth contact for pinion
- $P_D$ *is* the Hertzian contact pressure at the inner point $D$ of single pair tooth contact for wheel
- $\sigma_{H0}$ is the nominal contact stress at the pitch point C
- $Z_H$ is the zone factor
- $Z_E$ is the elasticity factor
- $Z_B$ is the pinion single pair tooth contact factor of the pinion
- $Z_D$ is the single pair tooth contact factor of the wheel
- $Z_\varepsilon$ is the contact ratio factor
- $Z_\beta$ is the helix angle factor (=1 for spur gear)
- $F_t$ is the nominal tangential load [N] (Equation (4)
- $d_1$ is the reference diameter of pinion [mm]

**Table 7**
Contact pressures ($P_C$, $P_B$, $P_D$), maximum shear stresses ($\tau_{max}$) and distance from the surface of $\tau_{max}$ ($z_{\tau max}$) for the two test conditions with torque of 200 Nm and 280 Nm.

| Description | Symbol | Unit | 200 Nm torque | 280 Nm torque |
|---|---|---|---|---|
| Pinion Torque | $T_1$ | *Nm* | 200 | 280 |
| **Pitch Contact Pressure** | $P_c$ | $MP_a$ | **1,020** | **1,208** |
| **Contact Pressure Single Pair pinion** | $P_b$ | $MP_a$ | **1,055** | **1,250** |
| **Contact Pressure Single Pair wheel** | $P_d$ | $MP_a$ | **1,045** | **1,238** |
| Zone Factor | $Z_H$ | (−) | 2,154 | 2,154 |
| Elasticity Factor | $Z_E$ | (−) | 170,902 | 170,902 |
| Contact ratio Factor | $Z_\varepsilon$ | (−) | 0.939 | 0.939 |
| Helix angle Factor | $Z_\beta$ | (−) | 1.000 | 1.000 |
| Single pair Pinion | $Z_B$ | (−) | 1.034 | 1.034 |
| Single pair Wheel | $Z_D$ | (−) | 1.024 | 1.024 |
| **Maximum Shear Stress** | $\tau_{max}$ | $MP_a$ | **317** | **375** |
| **Distance from the surface of $\tau_{max}$** | $z_{\tau max}$ | *mm* | **0.16** | **0.20** |

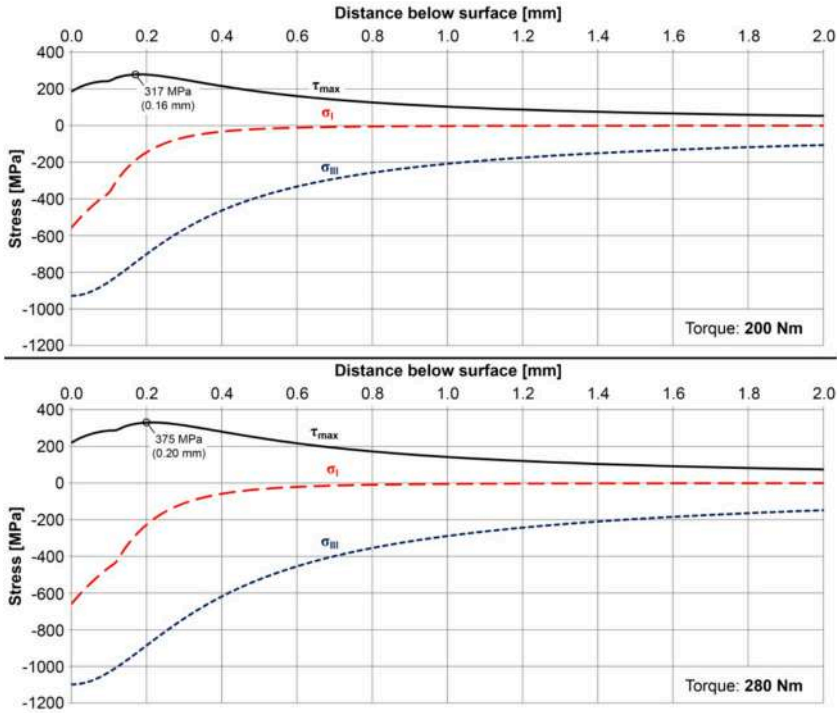


**Fig. 9.** Stress distribution in the contact zone varying the applied torque.

- $b$ is the face width [mm]
- $u$ is the gear ratio = $Z_2/Z_1$

Knowing the contact pressure and the contact half-width the principal stresses ($\sigma_I$, $\sigma_{III}$) and the maximum shear stress $\tau_{max}$ are calculated according to [46,47] and reported in Eqs. (7)–(9)):

$$\sigma_{III} = -P\frac{1}{\sqrt{1+\xi_b^2}}[MPa] \tag{7}$$

$$\sigma_I[MPa] = \begin{cases} -2\upsilon P\left[\sqrt{1+\xi_b^2} - |\xi_b|\right] for 0 \le \xi_b \le 0,436 \\ -P\left[\left(\frac{1+2\xi_b^2}{\sqrt{1+\xi_b^2}}\right) - 2|\xi_b|\right] for \xi_b \ge 0,436 \end{cases} \tag{8}$$

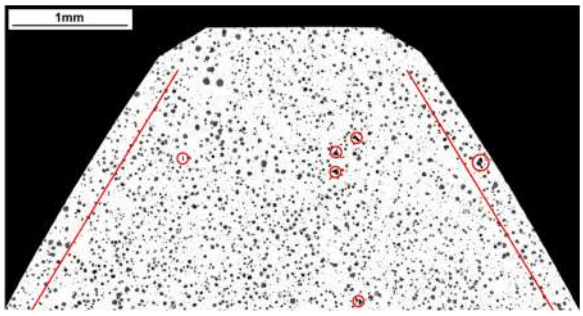


**Fig. 10.** Metallographic analysis of the head of a pinion tooth before etching: distribution and size of nodules. The red lines show the region where the maximum shear stress is expected when the applied torque is equal to 280 Nm, while the red circles highlights the casting defects. (For interpretation of the references to colour in this figure legend, the reader is referred to the web version of this article.). (For interpretation of the references to colour in this figure legend, the reader is referred to the web version of this article.)

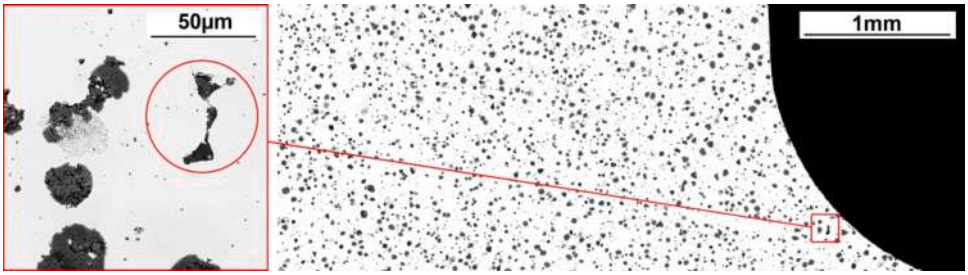


**Fig. 11.** Metallographic analysis of the root of a pinion tooth before etching: distribution and size of nodules. The red circle highlights a casting defect. (For interpretation of the references to colour in this figure legend, the reader is referred to the web version of this article.). (For interpretation of the references to colour in this figure legend, the reader is referred to the web version of this article.)

$$\tau_{max} = \frac{\sigma_I - \sigma_{III}}{2}[MPa] \tag{9}$$

where:

1. $\xi_b = \frac{z}{b_h}$ = nondimensional depth below the surface
2. $b_h$ = contact half-width
3. $\upsilon$ = Poisson's ratio
4. P=contact pressure

Table 7 shows contact the pressure and the shear stress values for the two load levels, 200Nm and 280Nm. The maximum contact pressure occurs at the inner point of single pair tooth contact of the pinion (Point B) for both the 200 Nm and 280 Nm torques. Point B is located in the pinion dedendum, also characterized by a negative sliding condition. Therefore, this area is the most critical for contact fatigue damage. In both cases the maximum shear stress refers to the maximum contact pressure $P_B$ which is equal to 1,055.8 MPa and 1,249.3 MPa for torques of 200 Nm and 280 Nm respectively. The highest shear values are equal to 316.6 MPa at 0.16 mm from surface and 375.1 MPa at 0.20 mm from surface for torques of 200 Nm and 280 Nm respectively.

Fig. 9 show the stresses below the contact zones for both the considered applied torques.

### 4.2. Metallographic analysis of the as-delivered gears

Figs. 10 and 11, obtained before etching, show the distribution of the graphite nodules in one of the observed teeth. It is quite homogenous without clusters. Some little casting defects (shrinkage cavities) are also present. They can anticipate the contact fatigue damage if they are positioned inside the region where the maximum shear stress is expected. For example, the red lines in Fig. 10 are drawn at about 0.20 mm from the surface, that is the distance at which the maximum shear stress is obtained when the applied torque is 280 Nm. Some of these defects are highlighted with red circles in Figs. 10 and 11 and one of them can be seen more in detail in Fig. 11.

By image analysis, the average diameter and roundness ($R = p^2/4\pi S - p$ and $S$ are the spheroid perimeter and area respectively) of the graphite spheroids were measured and the results are reported in Fig. 12.

Most of the graphite spheroids have an average diameter lower than 30 μm (about 90 %). Moreover, their morphology is pretty

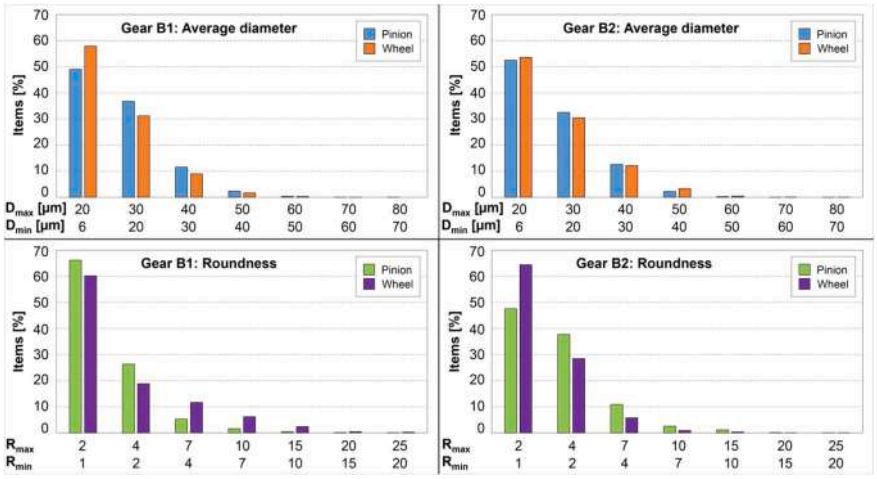


**Fig. 12.** Graphite nodules average diameter and roundness distribution in B1 and B2 gears.

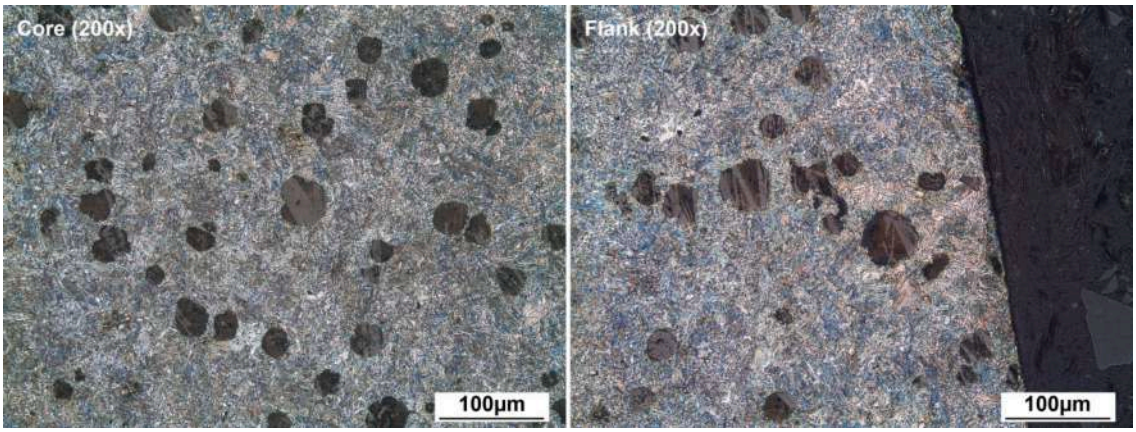


**Fig. 13.** Metallographic analysis of the core and flank of a pinion tooth after etching with Nital2. Etching highlights the typical ausferrite structure with homogeneous and dense network of ferrite needles surrounded by austenite.

good since the roundness value of about 60 % of them is lower than 2. This suggests that the large majority of the spheroids is small and round. Such information is very important from the fatigue mechanism point of view, because such characteristics minimize the influence of the graphite nodules on the crack nucleation.

The chemical etching highlights the typical ausferrite microstructure with homogeneous and dense network of ferrite needles surrounded by austenite as shown in Fig. 13.

### *4.3. Hardness tests*

Hardness is one of the most important parameters for contact fatigue life of gears [41]. According to Aslantas et al. [48], contact fatigue life increases when the austempering temperature decreases, since its decrease causes an increase of the tooth surface hardness. Furthermore, ADI are characterized by the TR.I.P. (TRansformation Induced Plasticity) effect. This causes an extra plasticity related to the austenite to martensite transformation when high pressure contacts are imposed to the surfaces and a hardness increase associated to the presence of martensite, thus resulting in an improved contact fatigue resistance. However, it is important to remember that ADI surface hardness is much lower than that of high-strength heat treated or carburized steels.

Two hardness methods were used on the same samples used for metallographic analysis. The first one was the Brinell method using a 2.5 mm WC ball and 187.5 kgf testing load, HBW2.5/187.5, and the second one was the Vickers method at a 500 gf load, HV0.5., in order to measure the hardness of the ausferritic matrix. The results, summarized in Table 8., agree with the JS-800-10 grade. The high standard deviation for HV0.5 tests is due to the small indentation size, which is conditioned by the difference in hardness of the two phases, austenite and ferrite, and by the presence of the graphite spheroids whose average distance is comparable with the imprint size.

**Table 8**
Experimental results of HV0.5 and HBW2.5/187.5 hardness tests performed on ADI JS-800–10. HV0.5 tests were performed only in the ausferritic matrix.

| **HBW2.5/187.5** | | **HV0.5** | |
|---|---|---|---|
| Mean | 307 | Mean | 307 |
| Dev. Std. | 4 | Dev. Std. | 64 |

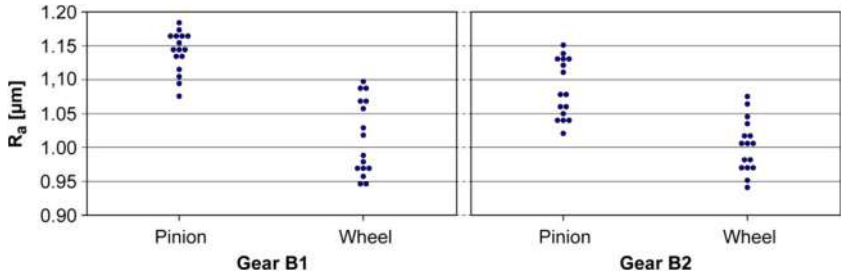


**Fig. 14.** Roughness values (Ra) measured before contact fatigue tests on four pinions and wheels teeth of gears B1 and B2.

### *4.4. Surface roughness*

The results of the surface analysis, graphically summarized in Fig. 14, are homogeneous without outliers. The mean value of $R_a$ between pinion and wheel seems to be different both for gear B1 and B2, but t-tests highlight that there is no statistical difference between them. Therefore, $R_a$ can be assumed to be about 1 µm for all gears, in complete agreement with the standard requirements for this type of application [49].

### *4.5. Visual examination of gear B1 tested with 200 Nm torque*

Fig. 15 shows the typical damage evolution of a tooth of pinion B1. The other damaged teeth showed similar damage evolution.

The surfaces of the tooth flanks always show pitting and spalling in the dedendum. These phenomena were expected, because this region was subject to the highest contact pressure, dynamic effects and negative sliding. The damage began in these areas from the early stages of the test and advanced steadily until its end. In these areas the surface is brighter, because the roughness was reduced by the interaction and the relative motion of the teeth flanks enhanced by possible breakage of the lubricant film. Failure started between $5.5{\cdot}10^6$ and $6.0{\cdot}10^6$ cycles from a pit on the tooth flank: the damage propagated rapidly until the final failure about $0.5{\cdot}10^6$ cycles after the pit nucleation. The very fast evolution is enhanced by the oil pressure penetrated inside the crack. The damage also spread rapidly to the teeth close to the one shown in Fig. 15; this phenomenon is due to the reduced load-bearing capacity of the tooth, which led to a load increase on the adjacent teeth.

Regarding the B1 wheel, Fig. 16 shows an example of the damage evolution observed on all teeth. The addendum and the dedendum areas showed initial pitting, but the damage remained stable and did not spread so quickly and destructively as in the pinion.

### *4.6. Visual examination of B2 gear tested with 280 Nm torque*

The B2 gear was monitored with the same procedure used for B1 gear. Increasing torque from 200 Nm to 280 Nm caused the surface to fail quickly and without warning (increased noise and vibrations). The damage level, in fact, was higher, changing from pitting to a severe spalling. Similarly to B1 gear, spalls are concentrated in the dedendum, but they are deeper than in the 200 Nm torque tests. This condition is a direct consequence of the increased contact pressure, which extends the distance from the surface at which the shear stress is maximum. As a result, deeper spalls form on the surface as can be seen in Figs. 17 and 18.

As in the test with the lower load, pitting was observed near the tip and the root of the tooth. Nevertheless, it is less prevalent, since the increased contact pressure has accelerated the propagation of the main cracks, leaving no time for the growth of other pits. The failure criteria (4 % damage of the tooth active area) on the pinion was reached soon, at 750,000 cycles, but remained almost stable until 1,300,000 cycles. However, the damage quickly spread to the adjacent teeth of the pinion and to one tooth of the wheel, as visible in Fig. 18.

### *4.7. Scanning electron microscope (SEM) analysis*

After the contact fatigue tests, samples cut from two teeth of the B1-200-L pinion and two teeth of the B2-280-L pinion, were observed in the SEM, as shown in Figs. 19 and 20. Cracks grow interacting with graphite nodules, leading to an irregular shape of the

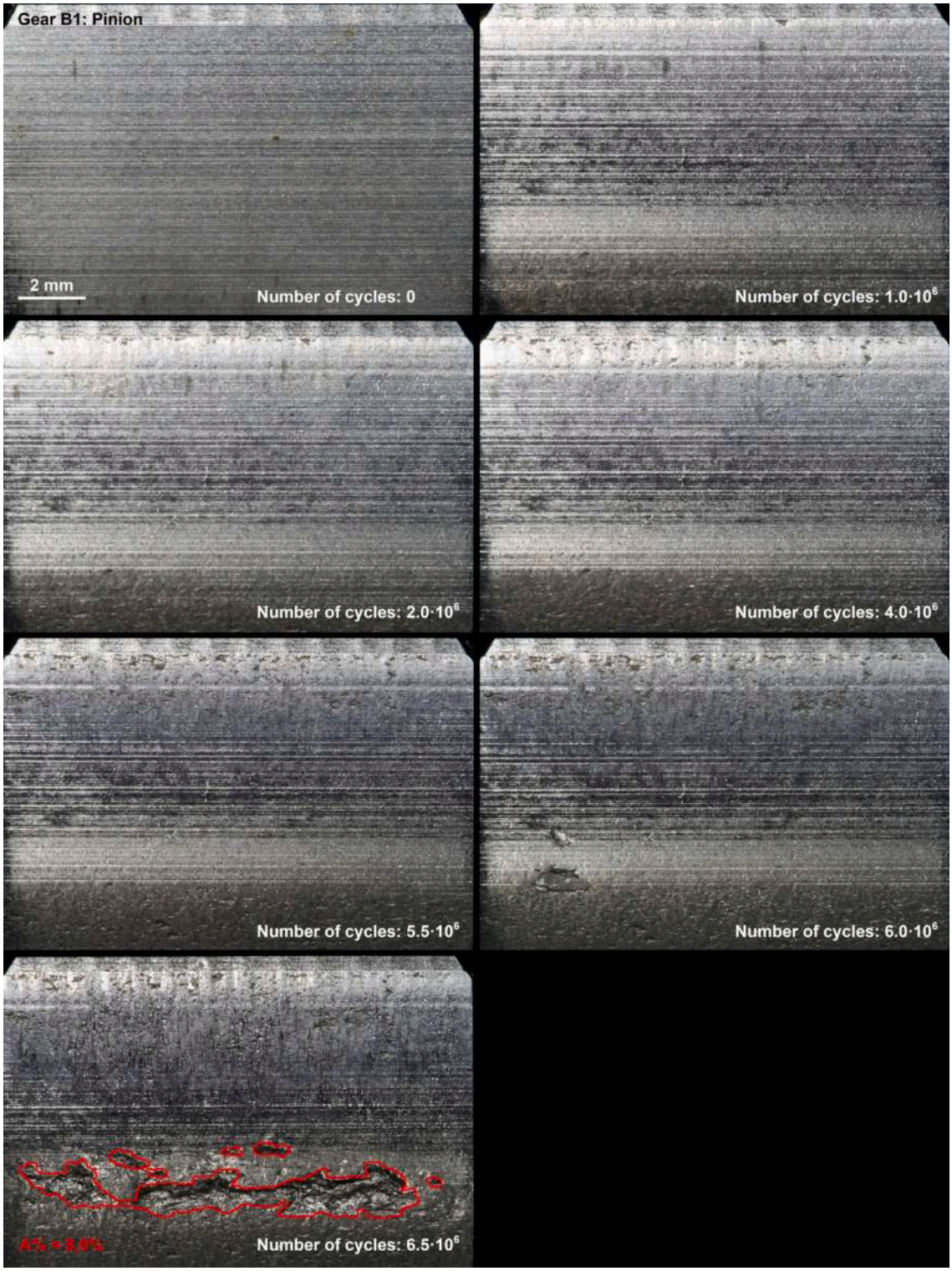


**Fig. 15.** Damage evolution of the most representative damaged tooth of pinion B1-200-L. Tests were regularly stopped to monitor the damage evolution of the tooth flank.

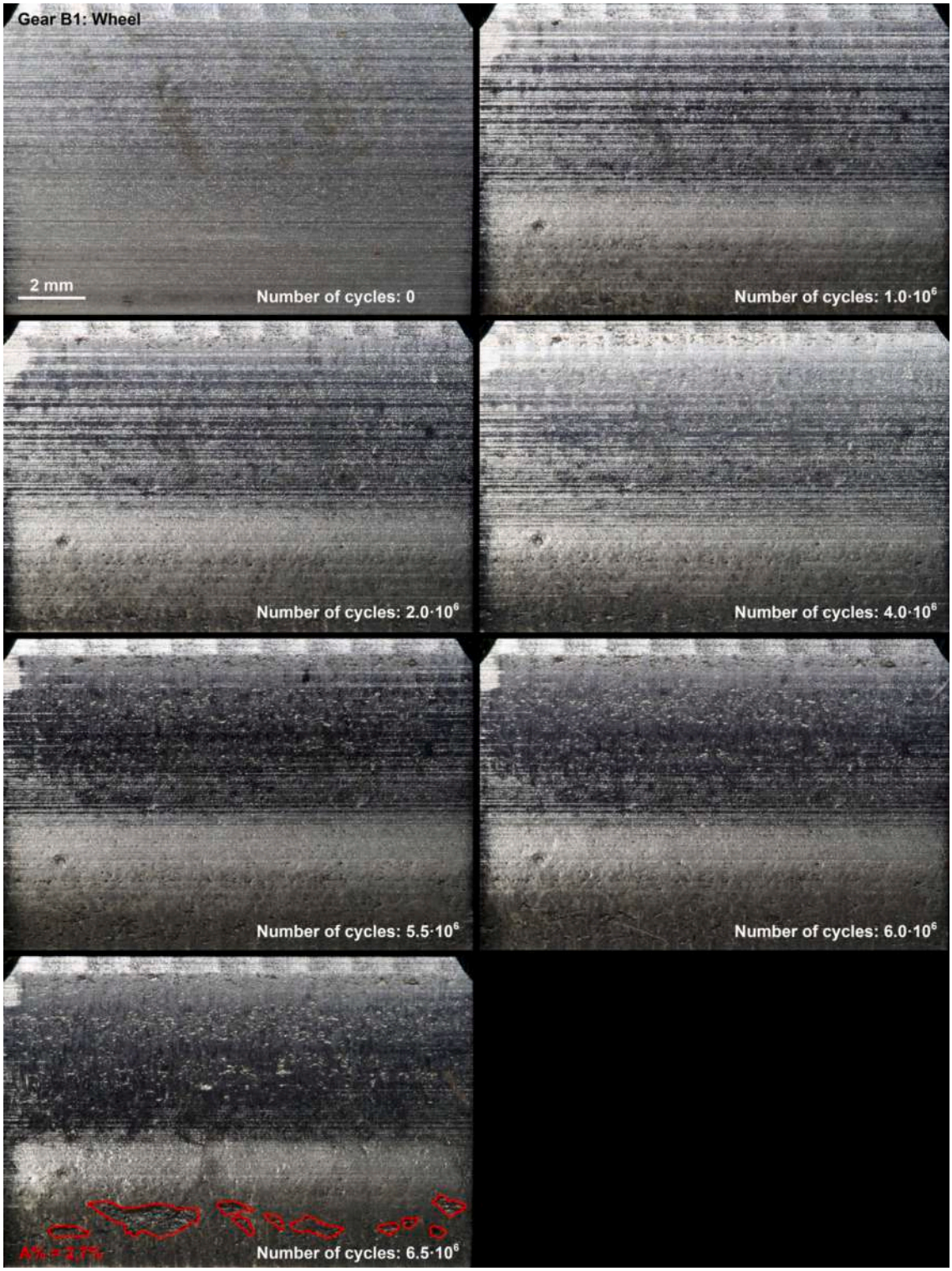


**Fig. 16.** Damage evolution of the most representative damaged tooth of wheel B1-200-L. Tests were regularly stopped to monitor the damage evolution of the tooth flank.

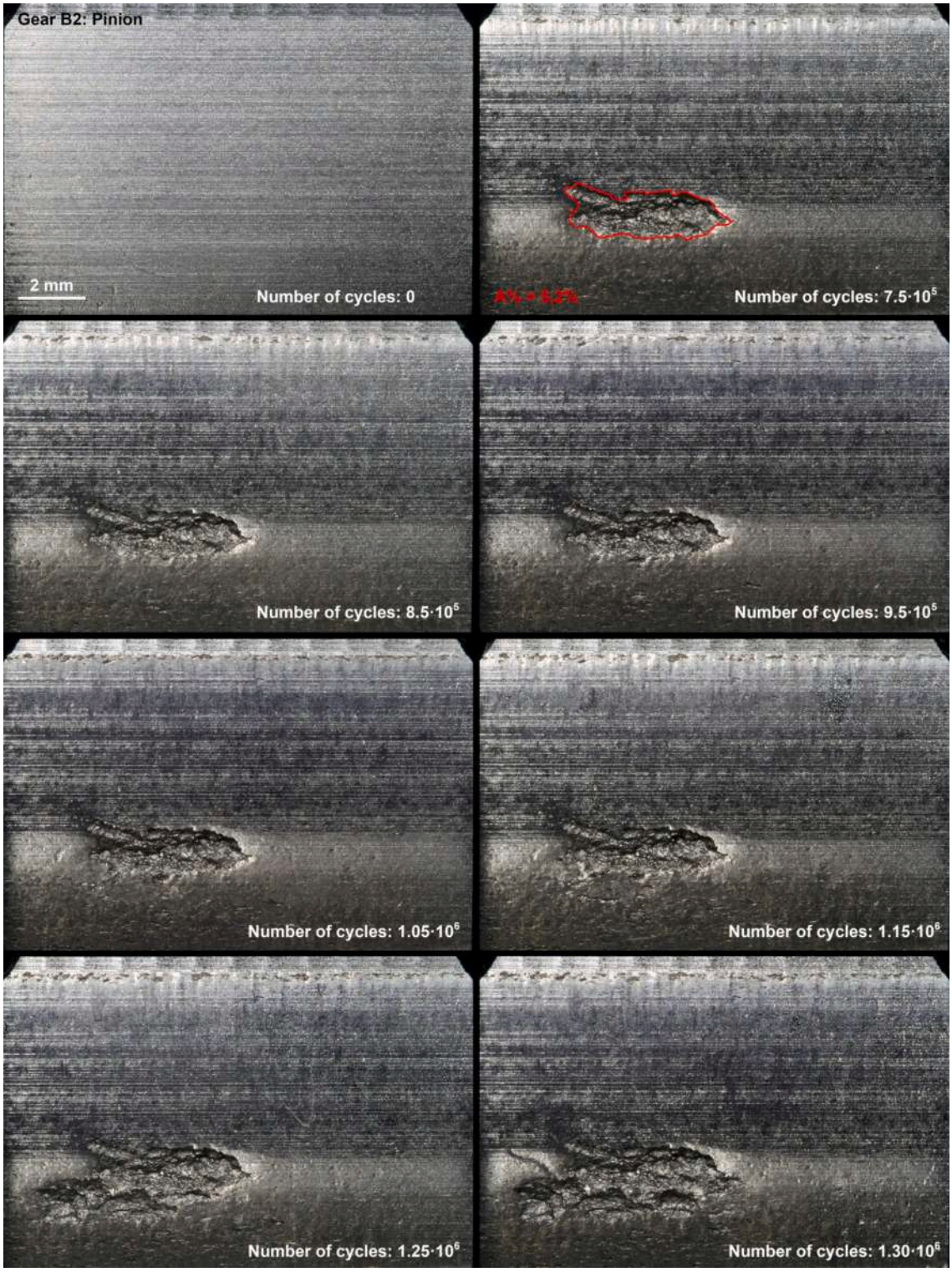


**Fig. 17.** Damage evolution of the most representative damaged tooth of pinion B2-280-L. Tests were regularly stopped to monitor the damage evolution of the tooth flank.

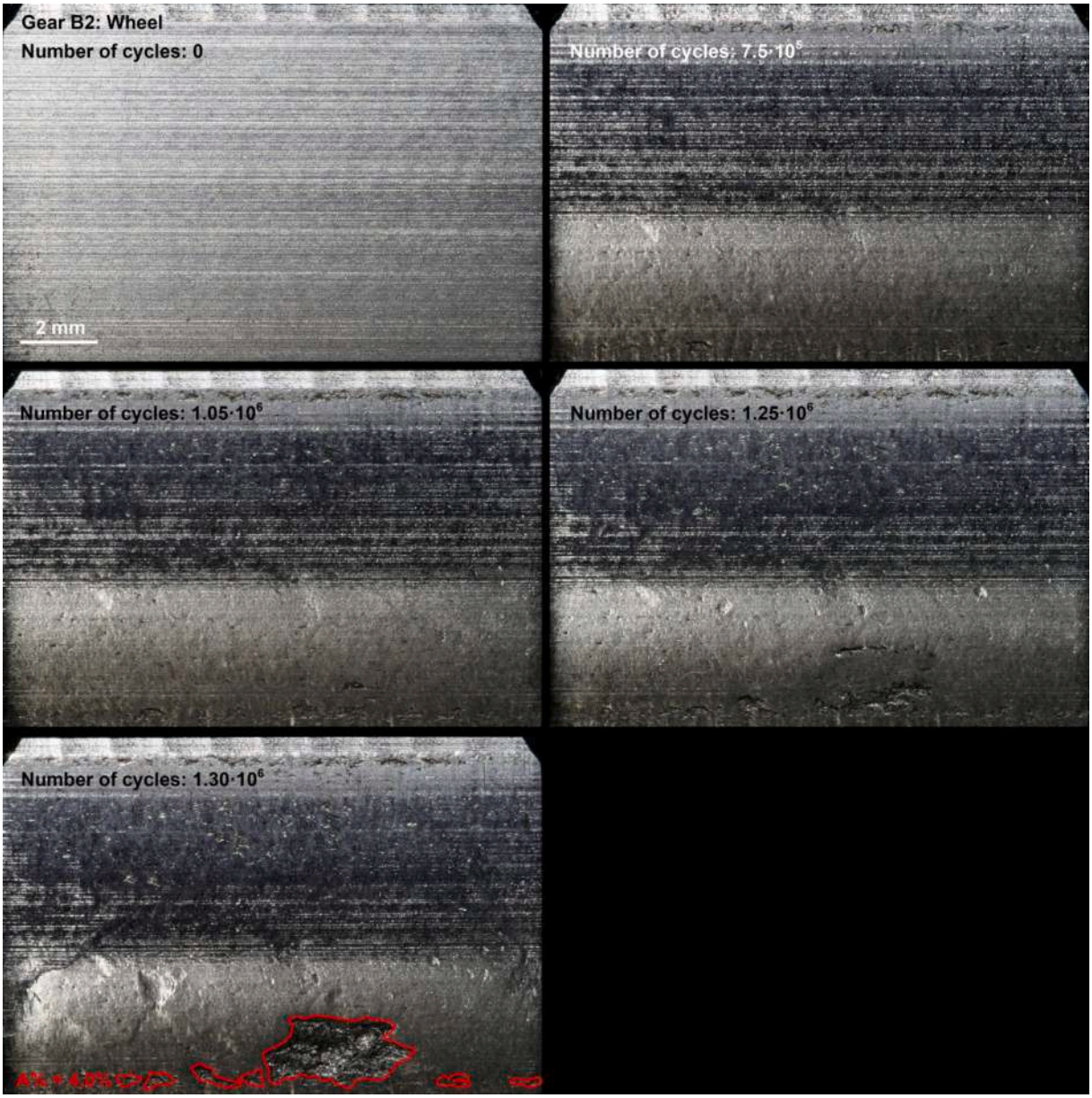


**Fig. 18.** Damage evolution of the most representative damaged tooth of wheel B2-280-L. Tests were regularly stopped to monitor the damage evolution of the tooth flank.

fracture surface, slightly different from the typical V-shape of hardened steel gears [50]. Both the addendum and dedendum show high plastic deformation of the surface, due to the friction force developed by the sliding conditions. In fact, moving away from the pitch line, the sliding speed increases and a more severe wear mechanism is activated [51] in addition to the contact fatigue stresses.

The material on the surface is smeared in the sliding direction and the grinding marks are completely removed. The shear stress resulting from sliding causes the material to flow over the craters and form a tapered edge on the exit side. The sliding direction also influences the crack orientation, indicated by the white arrows in Fig. 20. Such as the cracks propagation, also the plastic flow of the material on the teeth surface develops in an opposite direction in respect to the sliding one, as shown in Fig. 20 (right side).

Fig. 21 shows the rough aspect of a surface where the fatigue crack propagation occurs in a ductile material. Usually the pits form where there are graphite nodules or casting defects, near the surface as shown in Fig. 22. The smaller pits, in some cases, are completely covered by the plastic flow of the material.

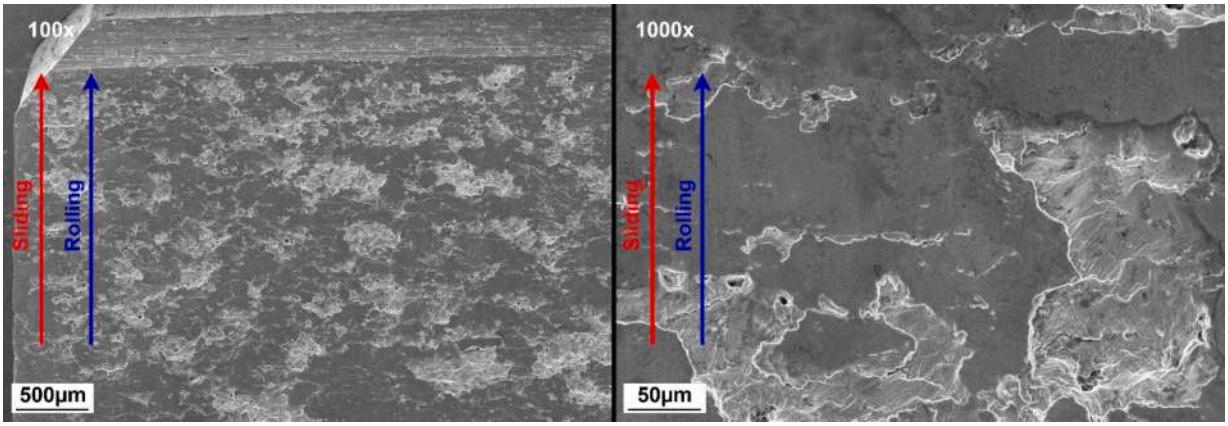


**Fig. 19.** Typical appearance of damaged tooth in pinion B1-200-L, showing pitting in the addendum.

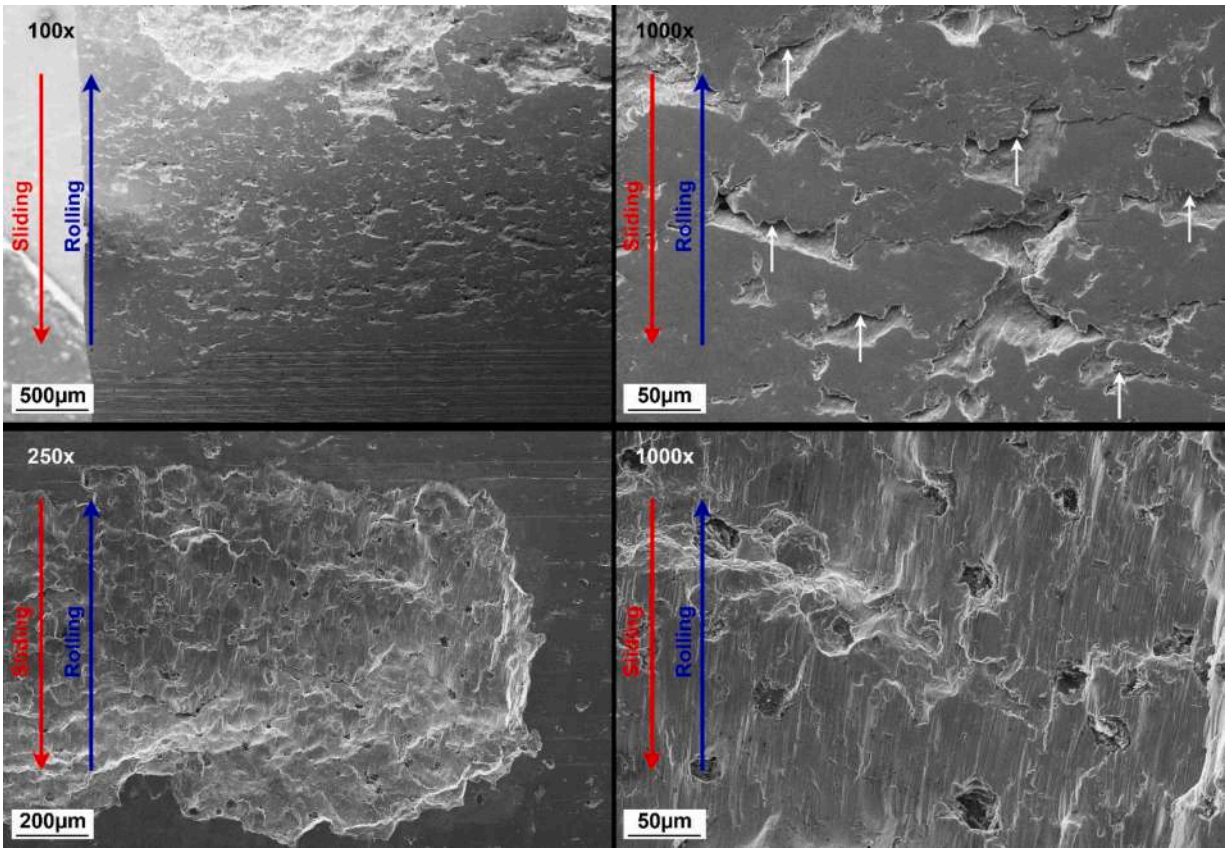


**Fig. 20.** Typical appearance of damaged tooth in B1-200-L pinion, showing high surface plastic deformation in the dedendum.

### *4.8. Sub-surface metallographic analysis of the tested gears*

Transverse sections of four teeth of B1-200-L gear pinion and four teeth of B2-280-L pinion, were analysed by optical microscopy up to 1 mm below the surface on teeth with different levels of damage, to better understand the mechanism of crack nucleation and propagation. The metallographic investigation provided important information on what happened in the sub-surface area of the gears, confirming what was observed in the SEM analysis. Fig. 23 shows that in the dedendum, cracks begin on the gear tooth surface and develop at an angle of 10° to 30° with respect to the surface, pointing towards the pitch line. In this region, breakage always begins between the initial single tooth meshing and the pitch line.

In the addendum, instead, the crack propagation direction changes, pointing towards the pitch line as shown in Fig. 24. The wheel

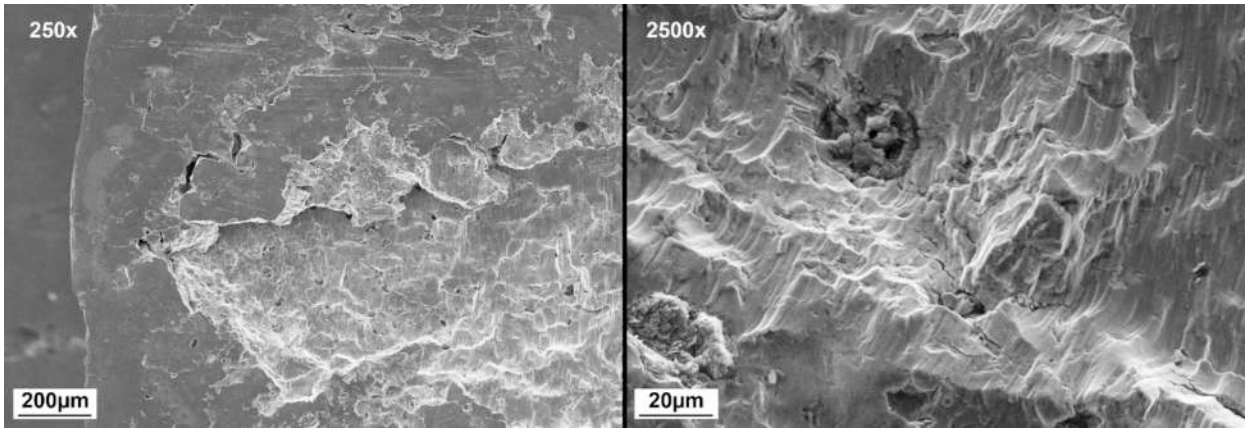


**Fig. 21.** Flank of the most representative damaged tooth of B1-200-L pinion. The image shows the surface of one spall, clearly visible on dedendum, when observed at high magnification.

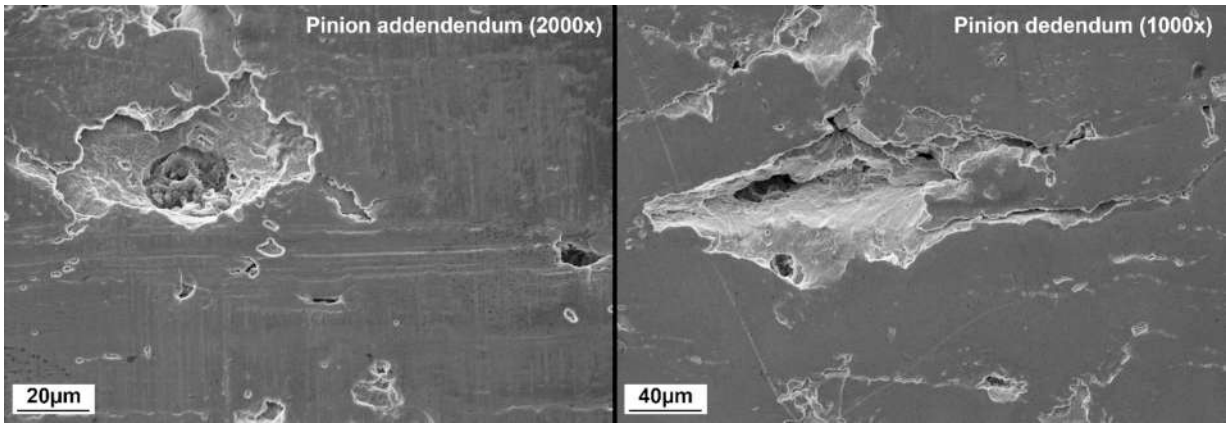


**Fig. 22.** Flank of the most representative damaged tooth of pinion B2-280-L. The image shows the formation of pits from graphite nodules or shrinkage cavities located just below the surface.

has the opposite behaviour.

As said before, sliding is detrimental, because it generates heat and reduces the efficiency, especially when its speed increases. Furthermore, negative sliding, which occurs in the dedendum, pumps oil in the surface cracks, accelerating their growth [52]. The tangential force, resulting from the relative sliding, generates a tensile stress on the surface. As a consequence, the crack mouth is opened and the oil can enter into the crack as described in Fig. 25a. Fig. 25b shows what happens when the contact zone covers the mouth of the crack: the oil hydraulic pressure is exerted on the crack faces inducing a tensile stress at its tip. As the contact area moves over the defect, the crack mouth closes because of the action of the friction forces, as shown in Fig. 25c. The oil is sealed inside and the crack opens again due to the oil squeezing out of the crack itself. This mechanism is not present in the addendum, because the rolling and the sliding speed have the same direction. The friction force, which has the same direction of the sliding speed, closes the crack before the oil can enter.

These considerations explain well what it is observed beneath the surface. Fig. 26 shows an initial stage of crack propagation. The cracks start from the surface and point towards the pitch line. These small flaws are formed by the high friction forces generated during the contact. The crack path is influenced by the graphite nodules generating a network as shown in Fig. 26.

Fig. 23 shows three consecutive pits. Cracks propagate beneath these pits following the initial propagation direction, strongly influenced by the notch effect associated to the pits and the shrinkage cavity under the second crater. The same behaviour can be observed in other teeth with higher damage level. All cracks begin at the tip of a macro-pit and grow deep from the surface. Moreover, crack propagation is affected by casting defects and graphite nodules. The depth of the macro-pits formed on the gears tested at 200 Nm torque ranges from 100 μm to 200 μm.

By increasing the load from 200 Nm to 280 Nm the fracture behaviour shows some differences. Cracks always start from the surface and develop at an angle included between 10° and 30° with respect to the surface, pointing towards the pitch line. Many cracks start from spalls and move parallel to the surface at a depth of about 200 μm, interacting with casting defects and graphite nodules. This distance matches with the region where the shear stress is maximum as calculated in paragraph 4.1. At the higher torque value of 280

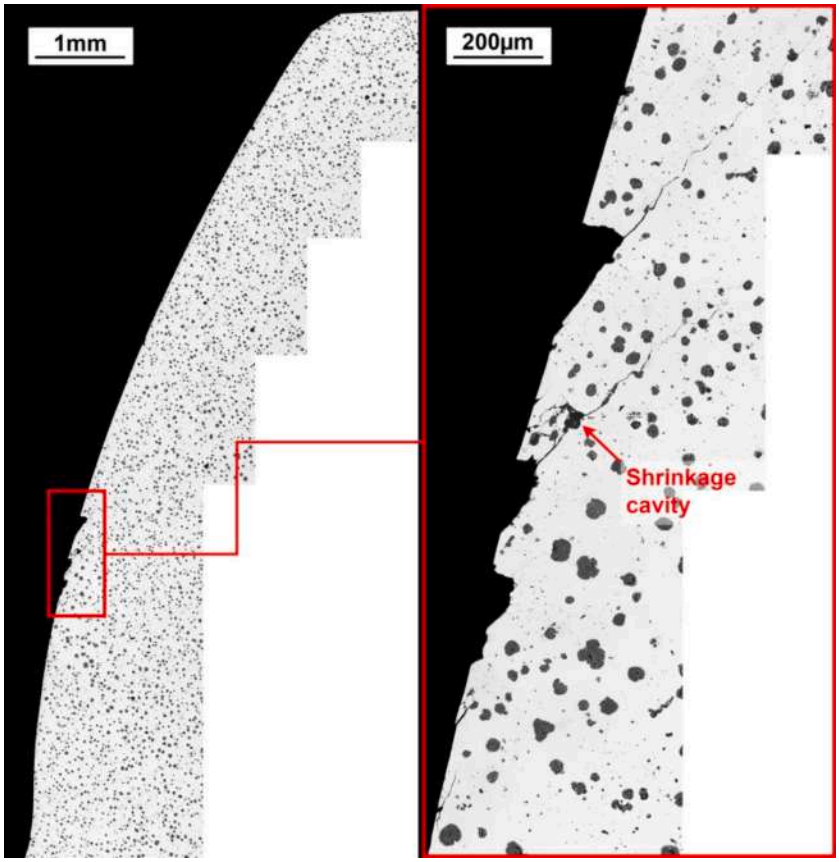


**Fig. 23.** Metallographic analysis on the most representative damaged tooth of pinion B1-200-L. The image shows that cracks begin on the gear tooth surface and develop at an angle of 10° to 30° with respect to the surface.

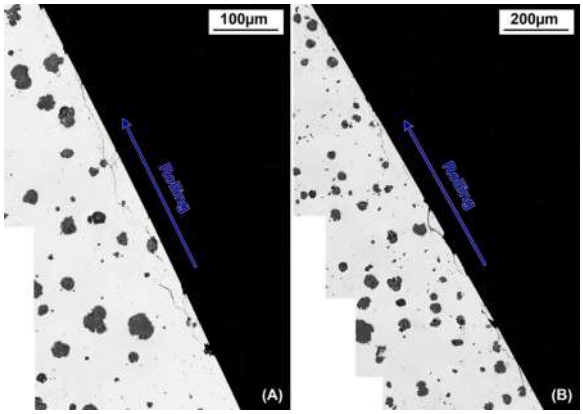


**Fig. 24.** Metallographic analysis on the most representative damaged tooth of pinion B1-200-R. The image shows the propagation direction of cracks formed in the addendum area.

Nm, the influence of Hertzian shear stress becomes more important, explaining why the damage propagated so rapidly. Another difference compared to the case with 200 Nm torque is the increase of the crack branching phenomenon.

As reported in Fig. 27, numerous small branches propagate from the main crack beneath the surface, interacting with the graphite nodules and the casting defects. The final spalls are deeper than those at 200 Nm, with depth ranging from 150 µm to 300 µm.

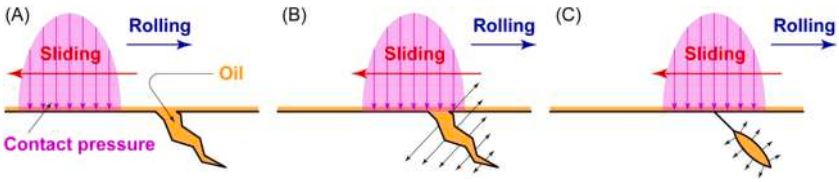


**Fig. 25.** Schematization of the hydraulic pressure action due to the negative sliding [46].

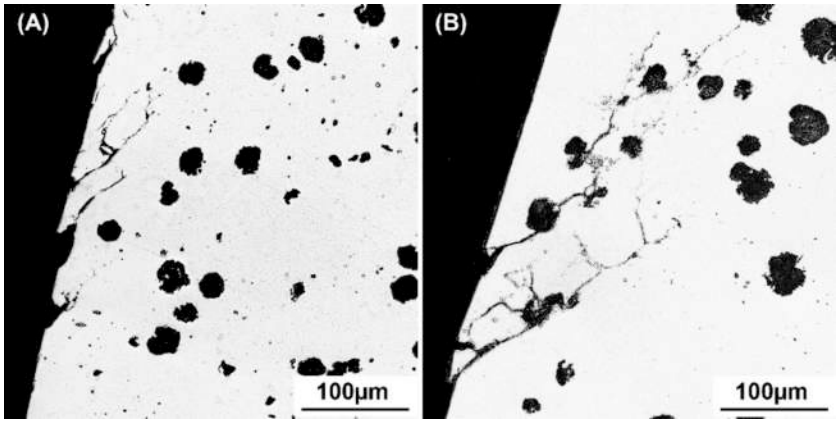


**Fig. 26.** Metallographic analysis on the most representative damaged tooth of pinion B1-200-L. The image shows the initial stage of crack propagation.

## 5. Conclusion

This work provided a better understanding of the mechanisms of contact fatigue-crack growth in Austempered Ductile Iron (ADI) spur gears. Based on the results obtained in the present experimental activity, the following conclusions can be listed:

- Gear failure always occurs first on the pinion than on the wheel. Wheel damage evolved more slowly. The main damaged area is always located between the initial point of single tooth pair contact and the pitch line.
- Cracks grow interacting with graphite nodules, leading to an irregular shape of the fracture surface, slightly different from the typical V-shape of hardened steel gears. Both the addendum and dedendum show high plastic deformation of the surface, due to the frictional force developed away from the pitch line, the only one area where pure rolling exists.
- The nucleation process of the cracks is related to the high stresses generated by the combination of rolling and sliding occurring on the tooth flank. These cracks can evolve and form pits and spalls. Cracks always begin at or near the gear tooth surface and grow at an angle of about $10^\circ - 30^\circ$ with respect to the surface. Pitting cracks grow in a direction opposite to the sliding one. Consequently, the cracks converge towards the pitch line of the pinion and diverge from the pitch line of the driven wheel.
- Negative sliding, in the gear dedendum, promotes damage propagation by allowing oil to enter inside the cracks.
- The crack propagation is enhanced by casting defects and graphite nodules, especially when they are clustered..
- Increasing the torque from 200 Nm to 280 Nm causes the surface to fail rapidly and without warning. The damage level, in fact, is higher changing from pitting to a severe spalling. The depth of the macro-pits formed on the gears tested at 200 Nm torque ranges from 100 μm to 200 μm. By increasing the load from 200 Nm to 280 Nm the fracture aspect changes. Many cracks start from spalls and move parallel to the surface at a distance of 200 μm where the shear stress reaches its maximum value. Compared with the lower torque value (200 Nm), when the load is higher (280Nm) the crack branching is enhanced. Numerous small branching cracks propagate beneath the surface, interacting with the graphite nodules and the casting defects. The final spalls are deeper than those at 200 Nm, with depth ranging from 150 μm to 300 μm.
- The base material must be of the highest quality as any casting defects can act as initiation site for crack development. The surface finishing must be of excellent quality as well, since cracks can originate from imperfections and surface irregularities.

## CRediT authorship contribution statement

**Andrea Casaroli:** Writing – original draft, Visualization, Validation, Supervision, Software, Investigation, Formal analysis, Data curation, Conceptualization. **Marco Boniardi:** Writing – review & editing, Supervision, Conceptualization. **Edoardo Conrado:** Validation, Investigation, Data curation, Conceptualization. **Carlo Gorla:** Writing – review & editing, Supervision, Conceptualization. **Carlo Crispino:** Conceptualization, Supervision, Writing – review & editing. **Riccardo Gerosa:** Writing – review & editing. **Barbara**

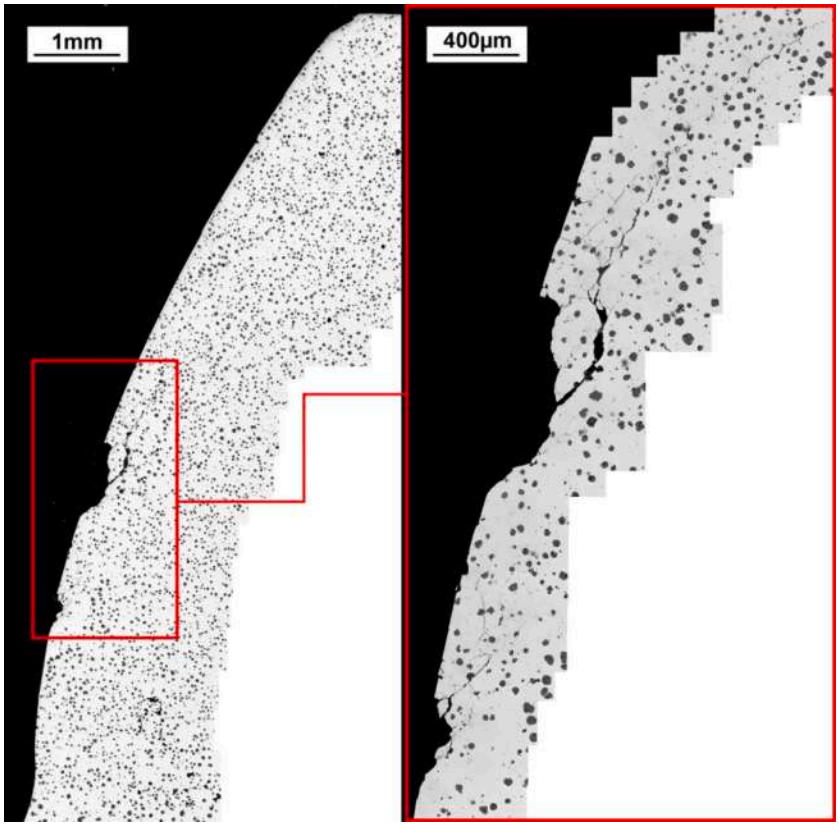


**Fig. 27.** Metallographic analysis on the most representative damaged tooth of pinion B2-280-L. The image shows numerous small branching cracks propagate beneath the surface instead of growing in the main direction, interacting with graphite nodules and casting defects.

**Rivolta:** Writing – review & editing.

## Declaration of competing interest

The authors declare that they have no known competing financial interests or personal relationships that could have appeared to influence the work reported in this paper.

## Data availability

The authors do not have permission to share data.

## References

[1] V. Rajinikanth, Manish Kumar Soni, B. Mahato, M. Ananda Rao, Microstructural investigation of rolling contact fatigue (RCF) on a failed planetary gear of a windmill gearbox, Eng. Fail. Anal. 121 (2021). ISSN 1350-6307.
[2] Wu Jiateng, Yu Yang, Junsheng Cheng, A novel estimation method of friction coefficient for evaluating gear pitting fault, Eng. Failure Anal. 129 (2021). ISSN 1350-6307.
[3] Zong Meng, Fulin Wang, Guixia Shi, A novel evolution model of pitting failure and effect on time -varying meshing stiffness of spur gears, Eng. Failure Anal. 120 (2021). ISSN 1350-6307.
[4] Yutao Yan, Cheng Jiang, Wendong Li, Simulation on coupling effects between surface wear and fatigue in spur gear, Eng. Failure Anal. 134 (2022). ISSN 1350-6307.
[5] M. Boniardi, A. Casaroli, L. Sirangelo, S. Monella, M. Mazzola, Failure analysis of boron steel components for automotive applications, Frattura Ed. Integrità Strutturale 17 (64) (2023) 137–147, https://doi.org/10.3221/IGF-ESIS.64.09.
[6] M. Boniardi, M. Guagliano, A. Casaroli, R. Andreotti, F. Ballerini, Large forgings: microstructural evolution and residual stresses due to quenching treatments - a combined numerical and experimental approach, Mater. Perform. Character. 3 (4) (2014) 118–136, https://doi.org/10.1520/MPC20130089.
[7] Masashi YAMANAKA, Yu MATSUSHIMA, Shinji MIWA, Yukihito NARITA, Katsumi INOUE, Yoshiki KAWASAKI, Comparison of Bending Fatigue Strength among Spur Gears Manufactured by Various Methods, Doi: 10.1299/jamdsm.4.480.
[8] L. Magalhaes, J.H. Seabra, Wear and scuffing of austempered ductile iron gears, Wear 215 (1998) 237–246, https://doi.org/10.1016/S0043-1648(97)00232-9.
[9] J. Han, G. Barber, Q. Zou, X. Sun, et al., Effect of material microstructure on scuffing behavior of ferrous alloys, SAE Tech. Paper 2011–01-1091 (2011), https://doi.org/10.4271/2011-01-1091.
[10] Masashi YAMANAKA, Ryo TAMURA, Katsumi INOUE, Yukihito NARITA, Bending Fatigue Strength of Austempered Ductile Iron Spur Gears, Journal of Advanced Mechanical Design, Systems, and Manufacturing, Doi: 10.1299/jamdsm.3.203.

[11] H.K.D.H. Bhadeshia, D.V. Edmonds, The bainite transformation in a silicon steel, Metall. Trans. A 10 (1979) 895–907, https://doi.org/10.1007/BF02658309.
[12] Y. Amran, Characterization and modeling of phase transition kinetics in austempered ductile iron, Technion-Israel Institute Technol. Depart. Mater. Eng. (2009).
[13] M. Nili-Ahmadabadi, H. Shirazi, Austempered ductile cast iron: Bainitic transformation, in: *Encyclopedia of Iron, Steel, and Their Alloys*, CRC Press, Boca Raton, FL, USA, 2015, pp. 217–230, https://doi.org/10.1081/E-EISA-120050833.
[14] G. Wenbang, C. Guodong, L. Jing, H. Li, Z. Zhonghe, Design and control of chemical compositions for high-performance austempered ductile iron, China Foundry (2012) 9.2.
[15] H.T. Angus, Cast iron: physical and engineering properties, Elsevier (2013), https://doi.org/10.1016/C2013-0-01035-3.
[16] A. Trudel, M. Gagne, Effect of composition and heat treatment parameters on the characteristics of austempered ductile irons, Canadian Meta. Quart. 36 (5) (1997) 289–298, https://doi.org/10.1016/S0008-4433(97)00028-1.
[17] Y. MI, Effect of Cu, Mo, Si on the content of retained austenite of austempered ductile iron, Scripta Metallurgica et Materialia 32 (9) (1995), https://doi.org/10.1016/0956-716X(95)00163-P.
[18] U. Zerbst, M. Madia, C. Klinger, D. Bettge, Y. Murakami, Defects as a root cause of fatigue failure of metallic components. III: Cavities, dents, corrosion pits, scratches, Eng. Failure Anal. 97 (2019) 759–776. ISSN 1350–6307.
[19] U. Zerbst, M. Madia, C. Klinger, D. Bettge, Y. Murakami, Defects as a root cause of fatigue failure of metallic components. II: Non-metallic inclusions, Eng. Failure Anal. 98 (2019) 228–239. ISSN 1350-6307.
[20] S.P. Radzevich, D.W. Dudley, Handbook of practical gear design, CRC Press (1994).
[21] J.R. Davis, Gear materials, properties, and manufacture, ASM Int. (2005), https://doi.org/10.31399/asm.tb.gmpm.9781627083454.
[22] L.E. Alban, Systematic analysis of gear failures, ASM Int. (1985), https://doi.org/10.31399/asm.tb.sagf.9781627084529.
[23] D.J. Wulpi, Understanding how components fail, ASM Int. (2013), https://doi.org/10.31399/asm.tb.uhcf3.9781627082709ù.
[24] H. Düzcükoğlu, H. Imrek, A new method for preventing premature pitting formation on spur gears, Eng. Fract. Mech. 75 (15) (2008) 4431–4438, https://doi.org/10.1016/j.engfracmech.2008.05.004.
[25] C. Moolwan, S. Netpu, Failure analysis of a two high gearbox shaft, Procedia-Social Behav. Sci. 88 (2013) 154–163, https://doi.org/10.1016/j.sbspro.2013.08.491.
[26] P.J.L. Fernandes, C. Mcduling, Surface contact fatigue failures in gears, Eng. Fail. Anal. 4 (2) (1997) 99–107, https://doi.org/10.1016/S1350-6307(97)00006-X.
[27] P.J.L. Fernandes, Tooth bending fatigue failures in gears, Eng. Failure Anal. 3 (3) (1996) 219–225, https://doi.org/10.1016/1350-6307(96)00008-8.
[28] C. Gorla, E. Conrado, F. Rosa, F. Concli, Contact and bending fatigue behaviour of austempered ductile iron gears, Proc. Institut. Mech. Eng., Part C: J. Mech. Eng. Sci. 232 (6) (2018) 998–1008, https://doi.org/10.1177/0954406217695846.
[29] Y. Murakami, Metal fatigue, Elsevier (2002), https://doi.org/10.1016/B978-0-08-044064-4.X5000-2.
[30] N. Rebasa, R. Dommarco, J. Sikora, Wear resistance of high nodule count ductile iron, Wear 253 (7–8) (2002) 855–861, https://doi.org/10.1016/S0043-1648(02)00171-0.
[31] R.C. Dommarco, A.J. Jaureguiberry, J.A. Sikora, Rolling contact fatigue resistance of ductile iron with different nodule counts and matrix microstructures, Wear 261 (2) (2006) 172–179, https://doi.org/10.1016/j.wear.2005.09.015.
[32] C.-K. Lin, P.-K. Lai, T.-S. Shih, Influence of microstructure on the fatigue properties of austempered ductile irons—I High-Cycle Fatigue, Int. J. Fatigue 18 (5) (1996) 297–307, https://doi.org/10.1016/0142-1123(96)82895-7.
[33] K. Aslantaş, S. Taşgetiren, A study of spur gear pitting formation and life prediction, Wear 257 (11) (2004) 1167–1175, https://doi.org/10.1016/j.wear.2004.08.005.
[34] G.L. Greno, J.L. Otegui, R.E. Boeri, Mechanisms of fatigue crack growth in austempered ductile iron, Int. J. Fatigue 21 (1999) 35–43, https://doi.org/10.1016/S0142-1123(98)00055-3.
[35] Gupta, V.; Bastias P.; Hahn G.T.; Rubin C.A., Influence of indent geometry on repeated two-dimensional rolling contact. **1995**: 655-659, Doi: 10.1115/1.2831531.
[36] L. Magalhães, J. Seabra, C. Sá, Experimental observations of contact fatigue crack mechanisms for austempered ductile iron (ADI) discs, Wear 246 (1-2) (2000) 134–148, https://doi.org/10.1016/S0043-1648(00)00493-2.
[37] L.L. Magalhães, J.O. Seabra, Contact properties of Cu-Mn austempered ductile iron gears. Experimental evaluation using the FZG test rig, VDI Berichte 1904 (2) (2005) 1145, https://doi.org/10.1016/j.wear.2007.05.007.
[38] E. Conrado, P.C. Davoli, C. Gorla, M. Guagliano, Progettazione a fatica degli ingranaggi, Organi Di Trasmissione 39 (8) (2008) 56–61.
[39] Gorla, C.; Conrado, E.; Rosa, F.; Concli, F., Austempered Ductile Iron (ADI) for gears: manufacturing, performances and tests. *International conference on gears 2017. VD IV DE-VERLAG GMBH*, **2017**, 977-988, Doi: 10.51202/9783181022948-977.
[40] Agma, 939–A07, Austempered ductile iron for gears, AGMA (2007).
[41] Iso, 17804:2020, Founding ausferritic spheroidal graphite cast irons classification, ISO (2020).
[42] T.C. Jao, Influence of surface roughness on gear pitting behavior, Gear Technol. (2006), https://doi.org/10.1177/0954406220931541.
[43] UNI EN ISO 21920-3:2022. Geometrical product specifications (GPS) - Surface texture: Profile - Part 3: Specification operators, ISO, **2022**.
[44] Valentin L. Popov, Markus Heß, Emanuel Willert, Handbook of Contact Mechanics, Springer Berlin, Heidelberg, Doi: 10.1007/978-3-662-58709-6.
[45] ISO 6336-2. Calculation of load capacity of spur and helical gears: Calculation of surface durability, ISO, **2006**.
[46] K.L. Johnson, Contact Mechanics. Cambridge University Press (1987), https://doi.org/10.1017/CBO9781139171731.
[47] Richard G. Budynas, J. Keith Nisbett, Shigley's Mechanical Engineering Design, McGraw-Hill Education, ISBN 9780071328401, Doi: 10.1115/1.3258702.
[48] K. Aslantaş, S. Taşgetiren, Y. Yalçin, Austempering retards pitting failure in ductile iron spur gears, Eng. Failure Anal. 11 (6) (2004) 935–941, https://doi.org/10.1016/j.engfailanal.2003.12.002.
[49] Y. Ding, N.F. Rieger, Spalling formation mechanism for gears, Wear 254 (12) (2003) 1307–1317, https://doi.org/10.1016/S0043-1648(03)00126-1.
[50] F. D'Errico, M. Boniardi, A. Casaroli, Danneggiamento per pitting di acciai bonificati, cementati e nitrurati, La Metallurgia Italiana 04 (2012) (2012) 05–11.
[51] ASM Handbook, Volume 18, Friction, Lubrication, and Wear Technology, George E. Totten, editor, DOI: 10.31399/asm.hb.v18.a0006396.
[52] Way, S., Pitting due to rolling contact, **1935**, A49-A58, Doi: 10.1115/1.4008607.